

Some recent improvements in meshfree methods for incompressible finite elasticity boundary value problems with contact

J.-S. Chen, H.-P. Wang, S. Yoon, Y. You

Abstract Two major difficulties are encountered in the meshfree solution of incompressible boundary value problems. The first is due to the employment of higher-order quadrature rules that leads to an over-constrained discrete system in incompressible problems. The second is associated with the treatment of essential boundary conditions and contact conditions owing to the loss of Kronecker delta properties in the meshfree shape functions. This paper discusses some recent enhancements in meshfree methods for incompressible boundary value problems, carries out numerical convergence analysis, and compares accuracy and efficiency improvement of these methods. Presented methods are a pressure projection method to remedy the over-constrained discrete system, and a mixed transformation method and a boundary singular kernel method for imposition of essential boundary conditions and contact constraints. Several linear and nonlinear problems were analyzed to demonstrate the effectiveness of the new approaches.

1

Introduction

The fully integrated displacement based lower-order finite elements are suffered by volumetric locking, which usually accompanies pressure oscillation, in incompressible problems. Methods that have been proposed under the finite element framework include, but are not limited to the mixed formulation (Herrmann 1965; Scharnhorst and Pian 1978; Belytschko and Bacharch 1986; Sussman and Bathe 1987; Liu et al. 1988; Atluri and Reissner 1989; Chang et al. 1991; Chen et al. 1996 a,b), the selective reduced integration method (Malkus and Hughes 1978), the hourglass control method on under-integrated elements (Flanagan and Belytschko 1981; Belytschko et al. 1984), the B-bar typed formulation (Hughes 1980; Simo et al. 1985; Liu et al. 1985), and pressure projection method (Chen et al. 1996a).

Recent advances in the development of meshfree methods provide attractive features in dealing with fracture (Belytschko et al. 1994, 1996a, b), multiple-scale (Liu et al. 1995, 1996a, b; Li et al. 1998), large deformation

hyperelasticity, plasticity, and contact problems (Chen et al. 1996b, 1997b, 1998), and the methods also provide high rate of convergence (Li et al. 1999; Atluri and Zhu 1998a, b) and are effective in implementing adaptivity procedures (Duarte and Oden 1995, 1996; Liszka et al. 1996; Melenk and Babuska 1996). It has been reported in Belytschko et al. (1994) and Chen et al. (1997b) that the meshfree methods formulated by the moving least-squares and reproducing kernel approximations are free of locking in incompressible problems; provided that a sufficiently large support size in the meshfree shape functions is employed in the formulation. This property makes some meshfree methods better choices than the conventional finite element methods for incompressible problems. However, the use of large support size in the meshfree shape functions significantly increases computational complexity in meshfree computation. Further, pressure oscillation cannot be removed with this approach (Chen et al. 1999a). A pressure projection method originally developed under the finite element framework (Chen et al. 1996a) was extended to a meshfree formulation (Chen et al. 1999a) to resolve locking and pressure oscillation difficulties in linear and nonlinear incompressible problems. In this approach, the pressure is projected onto a lower-order space locally at each integration zone to correct the over-constrained situation in the meshfree discretization of incompressible problems due to the use of higher-order quadrature rules. The employment of a full integration in the projection equation leads to an identical weak formulation to a perturbed Lagrangian mixed formulation (Sussman and Bathe 1987), and the use of a reduced integration in the pressure projection equation results in a form of selective reduced integration. This approach permits the use of a small support size in the meshfree shape functions for substantial efficiency improvement, and the method also resolves locking and pressure oscillation in incompressible problems.

Another cause of high CPU in the meshfree computation is due to the complexity involved in the treatment of boundary conditions. In general, the meshfree shape functions are not interpolation functions, and the discrete unknown variables are not expressed in nodal values. The Lagrange multiplier method is the most commonly used approach (Belytschko et al. 1994) to impose essential boundary conditions. With this approach, more unknown variables need to be solved, and the Babuska-Brezzi stability condition (Babuska 1973; Brezzi 1974) should be considered in the selection of shape functions for Lagrange multipliers. On the other hand, the transformation method

J.-S. Chen (✉), H.-P. Wang, S. Yoon, Y. You
Department of Mechanical Engineering,
The University of Iowa, 2137 SC, Iowa City, IA 52242-1527, USA

The Support of this work by NSF under the grant CMS 97-13842 and by NSF/DARPA OPAAL Program under the grant DMS 98-74015 to the University of Iowa is greatly acknowledged.

(Chen et al. 1996b, 1997b) provides a straightforward treatment for boundary conditions. The method is usually used in conjunction with the Lagrangian shape functions so that the transformation matrix and its inversion need to be computed only at the pre-processing stage in nonlinear computation. The efficiency of this method was later improved by introducing a mixed coordinate so that only the boundary nodes are expressed in nodal coordinates, and the size of the corresponding transformation matrix is proportional to the essential boundary degrees of freedom (Chen and Wang 1999b). Coupling with finite elements has also been introduced so that the essential boundary conditions can be imposed with the standard finite element procedures (Krongauz and Belytschko 1996). Another approach is to conduct D'Alembert's principle (Gunther and Liu 1998) with a Gram-Schmidt orthogonalization on boundary constraints and on the Jacobian of a coordinate transformation matrix for a reduced unconstrained matrix equation. A penalty method has also been used to yield a straightforward imposition of essential boundary conditions (Zhu and Atluri 1998). Introduction of singularity in the kernel functions leads to an interpolation function in MLS approximation (Lancaster and Salkauska 1981), and this property has been applied to the Element Free Galerkin (EFG) method (Kaljevic and Saigal 1997). However, some undesired convergence properties have been observed in this approach. A modification of this approach is to introduce singularity only to the essential boundary nodes to improve the accuracy while still maintaining the simplicity of the method (Chen and Wang 1999b).

The purpose of this paper is to discuss a few improved meshfree approaches for incompressible problems, and to perform a numerical convergence study of the pressure projection method and the boundary singular kernel method for incompressible finite elasticity applications. Section 2 reviews the reproducing kernel approximation that forms the basis of meshfree formulation. Section 3 discusses the fundamental difficulties in the meshfree formulation for nearly incompressible finite elasticity and introduces a pressure projection method for this class of problems. In Sect. 4, several boundary condition treatments for meshfree discretization are presented. The methods to impose contact constraints in contact problems are discussed in Sect. 5. Section 6 provides numerical analysis on the convergence properties of the pressure projection method and compares the accuracy and convergence of transformation and boundary singular kernel methods. Conclusions are given in Sect. 7.

2 Reproducing kernel approximation

2.1 Continuous reproducing kernel approximation

The reproducing kernel approximation (Liu et al. 1995) of a function $u(\mathbf{x})$ in a domain Ω_x is expressed by:

$$u^R(\mathbf{x}) = \int_{\Omega_x} u(\mathbf{s}) \bar{\Phi}_a^{[n]}(\mathbf{x}; \mathbf{x} - \mathbf{s}) d\mathbf{s} \quad (2.1)$$

where $u^R(\mathbf{x})$ is the reproduced function of $u(\mathbf{x})$, and $\bar{\Phi}_a^{[n]}(\mathbf{x}; \mathbf{x} - \mathbf{s})$ is a reproducing kernel of degree n with compact support measured by a dilation parameter a . To qualify as a reproducing kernel of degree n , the following reproducing kernel conditions need to be satisfied:

$$\int_{\Omega_x} s_1^i s_2^j s_3^k \bar{\Phi}_a^{[n]}(\mathbf{x}; \mathbf{x} - \mathbf{s}) d\mathbf{s} = x_1^i x_2^j x_3^k \quad \text{for } 0 \leq (i + j + k) \leq n \quad (2.2)$$

or equivalently,

$$\int_{\Omega_x} (x_1 - s_1)^i (x_2 - s_2)^j (x_3 - s_3)^k \bar{\Phi}_a^{[n]}(\mathbf{x}; \mathbf{x} - \mathbf{s}) d\mathbf{s} = \delta_{i0} \delta_{j0} \delta_{k0} \quad \text{for } 0 \leq (i + j + k) \leq n \quad (2.3)$$

A form of reproducing kernel proposed by Liu et al. (1995) is:

$$\bar{\Phi}_a^{[n]}(\mathbf{x}; \mathbf{x} - \mathbf{s}) = C^{[n]}(\mathbf{x}; \mathbf{x} - \mathbf{s}) \Phi_a(\mathbf{x} - \mathbf{s}) \quad (2.4)$$

and $C^{[n]}(\mathbf{x}; \mathbf{x} - \mathbf{s})$ is a correction function to impose reproducing conditions:

$$C^{[n]}(\mathbf{x}; \mathbf{x} - \mathbf{s}) = \sum_{i+j+k=0}^n (x_1 - s_1)^i (x_2 - s_2)^j (x_3 - s_3)^k b_{ijk}(\mathbf{x}) = \mathbf{b}^{[n]\top}(\mathbf{x}) \mathbf{H}^{[n]}(\mathbf{x} - \mathbf{s}) \quad (2.5)$$

In Eq. (2.5), $\mathbf{H}^{[n]}(\mathbf{x} - \mathbf{s})$ is a vector of n -th order monomial basis functions

$$\mathbf{H}^{[n]\top}(\mathbf{x} - \mathbf{s}) = [1, (x_1 - s_1), (x_2 - s_2), (x_3 - s_3), (x_1 - s_1)^2, \dots, (x_3 - s_3)^n] \quad (2.6)$$

and $\mathbf{b}^{[n]}(\mathbf{x})$ is the coefficient vector to be obtained from the reproducing conditions

$$\mathbf{b}^{[n]\top}(\mathbf{x}) = [b_{000}(\mathbf{x}), b_{100}(\mathbf{x}), b_{010}(\mathbf{x}), b_{001}(\mathbf{x}), b_{200}(\mathbf{x}), \dots, b_{00n}(\mathbf{x})] \quad (2.7)$$

Note that in Eq.(2.7) the coefficients are allowed to be functions of \mathbf{x} . Equation (2.3) can be rewritten as

$$\int_{\Omega_x} \mathbf{H}^{[n]}(\mathbf{x} - \mathbf{s}) \bar{\Phi}_a^{[n]}(\mathbf{x}; \mathbf{x} - \mathbf{s}) d\mathbf{s} = \mathbf{H}^{[n]}(\mathbf{0}) \quad (2.8)$$

Substituting Eqs. (2.4) and (2.5) into Eq. (2.8), $\mathbf{b}^{[n]}(\mathbf{x})$ can be obtained by

$$\mathbf{b}^{[n]}(\mathbf{x}) = \mathbf{M}^{[n]-1}(\mathbf{x}) \mathbf{H}^{[n]}(\mathbf{0}) \quad (2.9)$$

where

$$\mathbf{M}^{[n]}(\mathbf{x}) = \int_{\Omega_x} \mathbf{H}^{[n]}(\mathbf{x} - \mathbf{s}) \mathbf{H}^{[n]\top}(\mathbf{x} - \mathbf{s}) \Phi_a(\mathbf{x} - \mathbf{s}) d\mathbf{s} \quad (2.10)$$

Finally the continuous form of reproducing kernel approximation is obtained by

$$u^R(\mathbf{x}) = \mathbf{H}^{[n]\top}(\mathbf{0}) \mathbf{M}^{[n]-1}(\mathbf{x}) \times \int_{\Omega_x} \mathbf{H}^{[n]}(\mathbf{x} - \mathbf{s}) u(\mathbf{s}) \Phi_a^{[n]}(\mathbf{x}; \mathbf{x} - \mathbf{s}) d\mathbf{s} \quad (2.11)$$

2.2

Reproducing kernel shape functions

To derive the reproducing kernel shape functions for solving PDE's using the Galerkin method, the discrete reproducing kernel approximation is considered. Suppose the domain Ω_x is discretized by a set of nodes $\{\mathbf{x}_1, \mathbf{x}_2, \dots, \mathbf{x}_{NP}\}$, where \mathbf{x}_I is the position vector of node I , and NP is the total number of nodes. The discrete counterpart of the continuous reproducing kernel approximation (Eq. (2.1)) is

$$u^h(\mathbf{x}) = \sum_{I=1}^{NP} \bar{\Phi}_a^{[n]}(\mathbf{x}; \mathbf{x} - \mathbf{x}_I) d_I \equiv \sum_{I=1}^{NP} \Psi_I(\mathbf{x}) d_I \quad (2.12)$$

where $\Psi_I(\mathbf{x}) \equiv \bar{\Phi}_a^{[n]}(\mathbf{x}; \mathbf{x} - \mathbf{x}_I)$ is the reproducing kernel shape function, and $\bar{\Phi}_a^{[n]}(\mathbf{x}; \mathbf{x} - \mathbf{x}_I)$ is expressed by

$$\bar{\Phi}_a^{[n]}(\mathbf{x}; \mathbf{x} - \mathbf{x}_I) = C^{[n]}(\mathbf{x}; \mathbf{x} - \mathbf{x}_I) \Phi_a(\mathbf{x} - \mathbf{x}_I) \quad (2.13)$$

$$C^{[n]}(\mathbf{x}; \mathbf{x} - \mathbf{x}_I) = \mathbf{b}^{[n]\top}(\mathbf{x}) \mathbf{H}^{[n]}(\mathbf{x} - \mathbf{x}_I) \quad (2.14)$$

$$\mathbf{H}^{[n]\top}(\mathbf{x} - \mathbf{x}_I) = [1, (x_1 - x_{1I}), (x_2 - x_{2I}), (x_3 - x_{3I}), (x_1 - x_{1I})^2, \dots, (x_3 - x_{3I})^n] \quad (2.15)$$

For $\bar{\Phi}_a^{[n]}(\mathbf{x}; \mathbf{x} - \mathbf{x}_I)$ to qualify as a reproducing kernel of degree n , the following discrete reproducing conditions need to be satisfied:

$$\sum_{I=1}^{NP} x_{1I}^i x_{2I}^j x_{3I}^k \bar{\Phi}_a^{[n]}(\mathbf{x}; \mathbf{x} - \mathbf{x}_I) = x_1^i x_2^j x_3^k \quad \text{for } 0 \leq (i + j + k) \leq n \quad (2.16)$$

Equation (2.16) can be recast as

$$\sum_{I=1}^{NP} (x_1 - x_{1I})^i (x_2 - x_{2I})^j (x_3 - x_{3I})^k \bar{\Phi}_a^{[n]}(\mathbf{x}; \mathbf{x} - \mathbf{x}_I) = \delta_{i0} \delta_{j0} \delta_{k0} \quad \text{for } 0 \leq (i + j + k) \leq n \quad (2.17)$$

or

$$\sum_{I=1}^{NP} \mathbf{H}^{[n]}(\mathbf{x} - \mathbf{x}_I) \bar{\Phi}_a^{[n]}(\mathbf{x}; \mathbf{x} - \mathbf{x}_I) = \mathbf{H}^{[n]}(\mathbf{0}) \quad (2.18)$$

Substituting Eqs. (2.13) and (2.14) into (2.18), the coefficient vector $\mathbf{b}^{[n]}(\mathbf{x})$ can be obtained from the same equation in Eq. (2.9), only replacing $\mathbf{M}^{[n]}(\mathbf{x})$ by

$$\mathbf{M}^{[n]}(\mathbf{x}) = \sum_{I=1}^{NP} \mathbf{H}^{[n]}(\mathbf{x} - \mathbf{x}_I) \mathbf{H}^{[n]\top}(\mathbf{x} - \mathbf{x}_I) \Phi_a(\mathbf{x} - \mathbf{x}_I) \quad (2.19)$$

Combining Eqs. (2.12)–(2.14), and (2.19), finally the reproducing kernel shape function $\Psi_I(\mathbf{x})$ is obtained by

$$\begin{aligned} \Psi_I(\mathbf{x}) &\equiv \bar{\Phi}_a^{[n]}(\mathbf{x}; \mathbf{x} - \mathbf{x}_I) \\ &= \mathbf{H}^{[n]\top}(\mathbf{0}) \mathbf{M}^{[n]-1}(\mathbf{x}) \mathbf{H}^{[n]}(\mathbf{x} - \mathbf{x}_I) \Phi_a(\mathbf{x} - \mathbf{x}_I) \end{aligned} \quad (2.20)$$

3

Incompressible finite elasticity

3.1

Basic equations and fundamental difficulties

Consider an elastic solid initially occupies a domain Ω_X with a bounded surface Γ_X . Under the action of external forces, the elastic body deforms into a configuration with domain Ω_x and boundary Γ_x . The deformation of the solid is described by $\boldsymbol{\varphi}$. A point $\mathbf{X} \in \Omega_X$ in the initial configuration becomes a point with coordinate $\mathbf{x} = \boldsymbol{\varphi}(\mathbf{X}) \in \Omega_x$ after the deformation, and $\det \nabla \boldsymbol{\varphi}(\mathbf{X}) > 0$ for $\mathbf{X} \in \Omega_X$. Note that the displacement is $\mathbf{u}(\mathbf{X}) = \boldsymbol{\varphi}(\mathbf{X}) - \mathbf{X}$. A general form of an elasticity boundary value problem is

$$\inf \{ \Pi(\boldsymbol{\varphi}) : \boldsymbol{\varphi} = \mathbf{g} \quad \text{on} \quad \Gamma_X^g \} \quad (3.1)$$

with

$$\Pi(\boldsymbol{\varphi}) = \int_{\Omega_x} W(\nabla \boldsymbol{\varphi}(\mathbf{X})) d\Omega - W^{\text{ext}} \quad (3.2)$$

Here, $\Gamma_X^g \subset \Gamma_X$ is the essential boundary; the constraint $\boldsymbol{\varphi} = \mathbf{g}$ on Γ_X^g says that the deformation on Γ_X^g is a priori specified; $W(\nabla \boldsymbol{\varphi})$ is the stored strain energy density function; and W^{ext} is the external work done by the external forces. When the material is isotropic, the stored strain energy density function can be written in the form

$$W(\nabla \boldsymbol{\varphi}(\mathbf{X})) = W(I_1, I_2, I_3) \quad (3.3)$$

where I_1, I_2, I_3 are the three principal invariants of the Green deformation tensor $\mathbf{C} = \nabla \boldsymbol{\varphi}^\top \nabla \boldsymbol{\varphi}$, i.e.,

$$I_1 = \text{tr} \mathbf{C}; \quad I_2 = \text{tr}(\text{adj} \mathbf{C}); \quad I_3 = \det \mathbf{C} \quad (3.4)$$

The notation $\text{adj} \mathbf{C}$ denotes the transpose of the matrix of cofactors of \mathbf{C} . When \mathbf{C} is invertible, $\text{adj} \mathbf{C} = (\det \mathbf{C})^{-1} \mathbf{C}^{-\top}$. For nearly incompressible materials, it is more convenient to use reduced invariants

$$\bar{I}_1 = I_1 I_3^{-1/3} \quad \text{and} \quad \bar{I}_2 = I_2 I_3^{-2/3} \quad (3.5)$$

A deviatoric-volumetric decoupled strain energy density function is expressed by

$$W(\nabla \boldsymbol{\varphi}) = \bar{W}(\bar{I}_1, \bar{I}_2) + k \tilde{w}(J) \quad (3.6)$$

where $J = \det \nabla \boldsymbol{\varphi} = I_3^{1/2}$, and k is a penalty number to impose incompressibility. The reduced invariants \bar{I}_1 and \bar{I}_2 are measures of pure distortional (isochoric) deformation, J is related to volume change, and \bar{W} and $k \tilde{w}$ are referred to as the distortional and dilatational strain energy density functions, respectively. It has been shown (Chang et al. 1991) that the pressure is solely related to the dilatational strain energy density by

$$P = k \tilde{w}'(J) \quad (3.7)$$

One example of \tilde{w} is given by

$$\tilde{w}(J) = \frac{1}{2} (J - 1)^2 \quad (3.8)$$

and the corresponding pressure quantity is

$$P = k(J - 1) \quad (3.9)$$

To study the performance of meshfree method based on reproducing kernel approximation in nearly incompress-

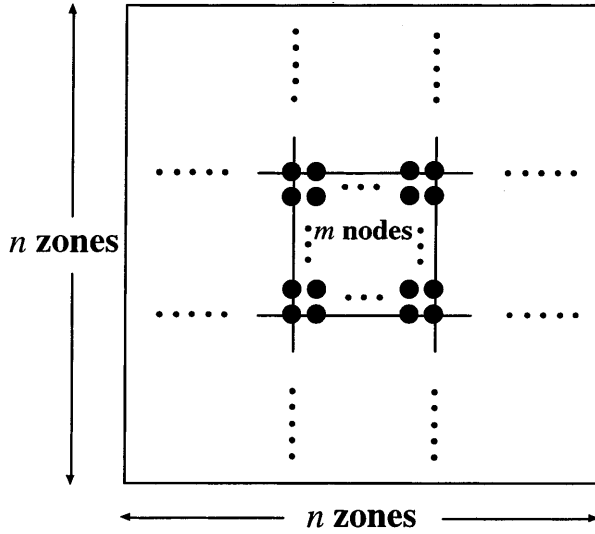


Fig. 1. Standard RKPM discretization

ible media, we introduce the method of constraint count (Hughes 1987). Let us introduce a rectangular domain partitioned into n integration zones per side, and each integration zone contains m nodes as shown in Fig. 1. A discrete constraint ratio r_c is defined by

$$r_c = \lim_{n \rightarrow \infty} \frac{N_{eq}}{N_c} \quad (3.10)$$

where N_{eq} is the number of discrete equilibrium equations, and N_c is the number of independent constraint equations. We want the discrete constraint ratio r_c to go toward the number of equilibrium equations divided by the number of incompressibility constraints in the continuum system when the number of discrete nodes approach infinity. Using an integration order of $(\sqrt{m} + 2) \times (\sqrt{m} + 2)$ (Belytschko et al. 1994), the pressure equation obtained from Eq. (3.9) is computed at each integration point \mathbf{x}_l :

$$P(\mathbf{x}_l) = k(J(\mathbf{x}_l) - 1) \quad \text{for } l = 1, \dots, (\sqrt{m} + 2)^2 \quad (3.11)$$

For nearly incompressible materials, $k \rightarrow \infty$, and for pressure to be bounded at each integration point the following condition must hold

$$J(\mathbf{x}_l) - 1 \approx 0 \quad \text{for } l = 1, \dots, (\sqrt{m} + 2)^2 \quad (3.12)$$

Equation (3.12) is the incompressibility constraint in finite elasticity. Note that in the iterative procedure of nonlinear computation, the linearized form corresponding to Eq. (3.12) is

$$J(\mathbf{x}_l) \Delta u_{i,i}(\mathbf{x}_l) \approx 0 \rightarrow \Delta u_{i,i}(\mathbf{x}_l) \approx 0 \quad \text{for } l = 1, \dots, (\sqrt{m} + 2)^2 \quad (3.13)$$

Equation (3.13) is analogous to the divergence free condition in incompressible linear elasticity. It is important to realize that the incompressibility constraints at the integration points are not necessarily linearly independent. The number of independent constraints of Eq. (3.13), n_c^k , of an integration zone Ω^k is determined by $n_c^k = \min(n_{int}^k, n_{ind}^k)$, where n_{int}^k is the number of in-

tegration points, and n_{ind}^k is the independency measure of $\{\Psi_{I,x}, \Psi_{I,y}\}_{I \in S^k}$ where S^k is a set of nodes with their corresponding reproducing kernel shape functions covering Ω^k . In the case of polynomials, the number n_{ind}^k can be directly computed. For example, in the case of 4-node finite element with bi-linear shape function that covers only up to the adjacent nodes and with 2×2 integration in each integration zone, $n_{int}^k = 4$, and $n_{ind}^k = 3$, and therefore there are only 3 independent constraints in each integration zone although 4 integration points are used. The discrete constraint ratio of this case is $r_c = 2/3$.

In the reproducing kernel approximation, the dependency of the discrete constraint equations is also influenced by the support size of the reproducing kernel shape functions. Consider a set of functions $\{f_a(\mathbf{x} - \mathbf{x}_I)\}_{I=1}^N$ with support measure "a". An indicator of the dependency of functions in $\{f_a(\mathbf{x} - \mathbf{x}_I)\}_{I=1}^N$ is the condition number the Gram matrix of $\{f_a(\mathbf{x} - \mathbf{x}_I)\}_{I=1}^N$. Here we consider the following functions

1. Linear function

$$f_a(x - x_I) = \begin{cases} 1 - \frac{|x - x_I|}{a} & 0 \leq \frac{|x - x_I|}{a} \leq 1 \\ 0 & \text{otherwise} \end{cases} \quad (3.14)$$

2. Exponential function

$$f_a(x - x_I) = \begin{cases} \frac{e^{-\frac{|x - x_I|}{a}} - e^{-1}}{1 - e^{-1}} & 0 \leq \frac{|x - x_I|}{a} \leq 1 \\ 0 & \text{otherwise} \end{cases} \quad (3.15)$$

3. Rational function

$$f_a(x - x_I) = \begin{cases} \frac{2}{1 + \frac{|x - x_I|}{a}} - 1 & 0 \leq \frac{|x - x_I|}{a} \leq 1 \\ 0 & \text{otherwise} \end{cases} \quad (3.16)$$

To demonstrate the dependency of functions $\{f_a(x - x_I)\}_{I=1}^N$, a total of 11 sampling points equally spaced in domain $0 \leq x \leq 1$ is used to define the center locations of $f(x - x_I)$ in Eqs. (3.14)–(3.16). The effect of normalized support size R (support a divided by the nodal distance) on the condition number (C_G) of Gram matrix \mathbf{G} , $G_{IJ} = \int_0^1 f_a(x - x_I) f_a(x - x_J) dx$, for three functions are shown in Fig. 2. A larger condition number indicates a higher degree of dependency in $\{f_a(x - x_I)\}_{I=1}^N$. For the case of a linear function, it is clear that if a point is covered by

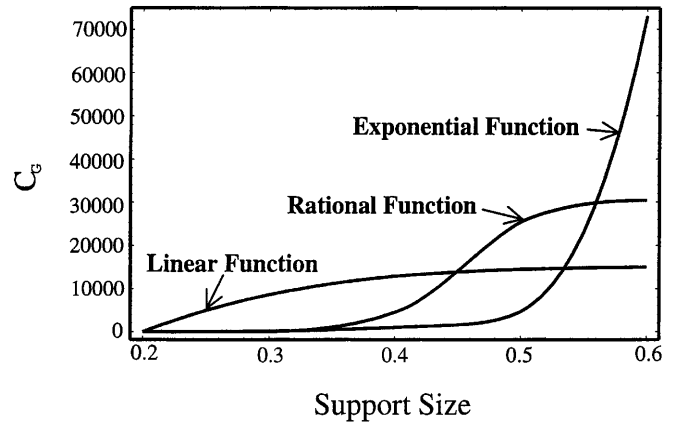


Fig. 2. The effect of support size on the condition numbers of a set of functions $\{f_a(x - x_I)\}_{I=1}^N$

more than two linear functions, only two of which are linearly independent. Therefore, dependency exists when $a > \Delta x$ and dependency increases as a increases. The curves of exponential and rational functions also show that the increase of support size leads to the increase of dependency.

The commonly used $(\sqrt{m} + 2) \times (\sqrt{m} + 2)$ integration order in the meshfree stiffness integration, with m the number of nodes in each integration zone as shown in Fig. 1, leads to a constraint ratio of $r_c = 2(\sqrt{m} - 1)^2 / [(\sqrt{m} + 2)^2 - n_d]$, where n_d is the number of dependent constraint equations that is related to the degree of dependency in $\{\Psi_{1,x}, \Psi_{1,y}\}_{I \in S^k}$. In the case of meshfree domain partitioning using a 4-node integration zone, the constraint ratio is $r_c = 2/(16 - n_d)$ and one needs to significantly increase the dependency of the discrete constraint equations to avoid locking. This can be achieved by increasing the support size of the reproducing kernel shape functions to increase the dependency of $\{\Psi_{1,x}, \Psi_{1,y}\}_{I \in S^k}$ as shown in Fig. 2. This approach avoids locking as has been observed in (Chen et al. 1997b), however it comes with a cost of an intensive computation and ill-conditioning in the stiffness matrix. Of course using $m \rightarrow \infty$ results in an optimum constraint ratio but the approach is not practical.

3.2 L_2 pressure projection

The number of independent constraint equations in each integration zone can be reduced by projecting displacement calculated pressure (Eq. (3.11)) onto a lower-order space. Concerning the most over-constrained situation when each integration zone contains 3 or 4 nodes, only one independent constraint equation is allowed to enhance the discrete constraint ratio to 1 and 2 for 3-node and 4-node integration zones, respectively. Recall the potential energy in Eq. (3.2), for which the stationary condition is

$$\delta \Pi = \int_{\Omega_x} \delta F_{ij} \frac{\partial \bar{W}}{\partial F_{ij}} d\Omega + \int_{\Omega_x} \delta F_{ij} (P J F_{ij}^{-1}) d\Omega - \delta W^{\text{ext}} = 0 \quad (3.17)$$

An L_2 projection of pressure $k(J - 1)$ to a constant field in each integration zone Ω_x^s is to minimize

$$\Theta(P^s) = \|k(J - 1) - P^s\|_{L_2(\Omega_x^s)}^2 \quad (3.18)$$

where $\|\cdot\|_{L_2(\Omega_x^s)}$ is the L_2 norm in the integration zone Ω_x^s . The minimization of $\Theta(P^s)$ leads to

$$P^s = \frac{k \int_{\Omega_x^s} (J - 1) d\Omega}{A^s} \quad (3.19)$$

The pressure in Eq. (3.19) is projected onto a constant field. Further taking the linearization of the variation of potential energy leads to

$$\begin{aligned} \Delta \delta \Pi = & \int_{\Omega_x} \delta F_{ij} \frac{\partial^2 \bar{W}}{\partial F_{ij} \partial F_{kl}} \Delta F_{kl} d\Omega \\ & + \int_{\Omega_x} \delta F_{ij} \left(P \frac{\partial J F_{ij}^{-1}}{\partial F_{kl}} \right) \Delta F_{kl} d\Omega \end{aligned}$$

$$+ \int_{\Omega_x} \delta F_{ij} J F_{ij}^{-1} \Delta P d\Omega - \Delta \delta W^{\text{ext}} \quad (3.20)$$

Similarly, in each integration zone Ω_x^s we project the pressure increment onto a constant field by an L_2 projection by minimizing

$$\hat{\Theta}(\Delta P^s) = \left\| kJ \frac{\partial \Delta u_i}{\partial x_i} - \Delta P^s \right\|_{L_2(\Omega_x^s)}^2 \quad (3.21)$$

By minimizing $\hat{\Theta}$ and introducing the reproducing kernel shape functions for displacement $\Delta \mathbf{u}$, one obtains the projected pressure in Ω_x^s

$$\Delta P^s = \frac{k \int_{\Omega_x^s} \mathbf{g} \mathbf{B} d\Omega}{A^s} \Delta \mathbf{d} \quad (3.22)$$

where \mathbf{g} is the row vector form of $J F_{ij}^{-1}$ and \mathbf{B} is the gradient matrix associated with the deformation gradient constructed using reproducing kernel shape functions. Note that Eq. (3.22) is the linearization of Eq. (3.19). In the incremental solution update process, the unbalanced pressure in Eq. (3.19) is added to the right side of Eq. (3.22) for pressure updating. The tangential stiffness matrix and internal force vector are obtained by introducing the displacement shape functions and substituting the projected P and ΔP in Eqs. (3.19) and (3.22) into the variational equation in Eq. (3.17) and its linearization in Eq. (3.20) to result in

$$\begin{aligned} \mathbf{K}_{IJ}^s = & \int_{\Omega_x^s} \mathbf{B}_I^T (\bar{\mathbf{C}} + \tilde{\mathbf{C}}^1) \mathbf{B}_J d\Omega \\ & + k A^{s-1} \left(\int_{\Omega_x^s} \mathbf{B}_I^T \mathbf{g}^T d\Omega \right) \left(\int_{\Omega_x^s} \mathbf{g} \mathbf{B}_J d\Omega \right); \end{aligned} \quad (3.23)$$

$$(\mathbf{f}^{\text{int}})_I^s = \int_{\Omega_x^s} \mathbf{B}_I^T (\bar{\boldsymbol{\sigma}} + \tilde{\boldsymbol{\sigma}}) d\Omega \quad (3.24)$$

where the notation $(\cdot)_{IJ}^s$ denotes the stiffness matrices associated with particle I, J integrated over the integration zone Ω_x^s , $\bar{\mathbf{C}}, \tilde{\mathbf{C}}^1, \bar{\boldsymbol{\sigma}},$ and $\tilde{\boldsymbol{\sigma}}$ are associated with $\partial^2 \bar{W} / \partial F_{ij} \partial F_{kl}$ and $P \partial (J F_{ij}^{-1}) / \partial F_{kl}, \partial \bar{W} / \partial F_{ij},$ and $P J F_{ij}^{-1}$, respectively, with P updated using Eq. (3.19)-(3.20). Note that with a constant pressure projection, the discrete constraint ratio is 1 for a 3-node integration zone, and is 2 for a 4-node integration zone. One way to further increase the discrete constraint ratio for a 3-node integration zone is to increase displacement degrees of freedom by adding points into each triangular integration zone.

The pressure projection formulation can be degenerated to linear elasticity by setting $F_{ij} \rightarrow \delta_{ij}$ and using the relationship of shear modulus $\mu = 2(A_{10} + A_{01})$ to yield

$$\mathbf{K}_{IJ}^s = \int_{\Omega_x^s} \mathbf{B}_I^T \bar{\mathbf{C}} \mathbf{B}_J d\Omega + k A^{s-1} \mathbf{b}_I^T \mathbf{b}_J \quad (3.25)$$

where $k = \lambda + 2\mu/3$, λ and μ are Lamé constants, and

$$\mathbf{b}_I = \int_{\Omega_x^s} [\Psi_{I,x}, \Psi_{I,y}] d\Omega \quad (3.26)$$

$$\bar{\mathbf{C}}_{ijkl} = \mu [\delta_{ik} \delta_{jl} + \delta_{il} \delta_{jk} - \frac{2}{3} \delta_{ij} \delta_{kl}] \quad (3.27)$$

4 Treatments of essential boundary conditions

4.1 Full transformation method

Due to the lack of Kronecker delta properties in the reproducing kernel shape functions in Eq. (2.20), the essential boundary conditions need to be introduced with additional effort. Using the Lagrangian reproducing kernel shape functions (Chen et al. 1996b), the kinematic admissible displacement $u_i^h(\mathbf{X})$ of the variational equation requires the satisfaction of the following conditions:

$$\left. \begin{aligned} u_i^h(\mathbf{X}_J) &= \sum_{I=1}^{NP} \Psi_I(\mathbf{X}_J) d_{iI} = g_i(\mathbf{X}_J) \\ \delta u_i^h(\mathbf{X}_J) &= \sum_{I=1}^{NP} \Psi_I(\mathbf{X}_J) \delta d_{iI} = 0 \end{aligned} \right\} \quad \forall \mathbf{J} \in \eta_{g_i} \quad (4.1)$$

where η_{g_i} denotes a set of particle numbers in which the associated particles are located on $\Gamma_X^{g_i}$. Equation (4.1) represents two sets of constraint equations that need to be solved simultaneously with the equilibrium equation. A transformation between the nodal value $u_i^h(\mathbf{X}_J) \equiv \hat{d}_{ij}$ and the “generalized” displacement d_{ij} can be established by

$$\hat{d}_{ij} = \sum_{I=1}^{NP} \Psi_I(\mathbf{X}_J) d_{iI} \quad (4.2)$$

or

$$\hat{\mathbf{d}} = \mathbf{\Lambda} \mathbf{d} \quad (4.3)$$

where

$$\hat{\mathbf{d}} = \begin{bmatrix} u_1^h(\mathbf{X}_1) \\ u_2^h(\mathbf{X}_1) \\ u_1^h(\mathbf{X}_2) \\ u_2^h(\mathbf{X}_2) \\ \vdots \\ u_1^h(\mathbf{X}_{NP}) \\ u_2^h(\mathbf{X}_{NP}) \end{bmatrix}; \quad \mathbf{d} = \begin{bmatrix} d_{11} \\ d_{21} \\ d_{12} \\ d_{22} \\ \vdots \\ d_{1NP} \\ d_{2NP} \end{bmatrix} \quad (4.4)$$

$$\mathbf{\Lambda} = \begin{bmatrix} \mathbf{A}_1^{1T} \\ \mathbf{A}_1^{2T} \\ \mathbf{A}_2^{1T} \\ \mathbf{A}_2^{2T} \\ \vdots \\ \mathbf{A}_{NP}^{1T} \\ \mathbf{A}_{NP}^{2T} \end{bmatrix}; \quad \mathbf{A}_J^1 = \begin{bmatrix} \Psi_1(\mathbf{X}_J) \\ 0 \\ \Psi_2(\mathbf{X}_J) \\ 0 \\ \vdots \\ \Psi_{NP}(\mathbf{X}_J) \\ 0 \end{bmatrix}; \quad \mathbf{A}_J^2 = \begin{bmatrix} 0 \\ \Psi_1(\mathbf{X}_J) \\ 0 \\ \Psi_2(\mathbf{X}_J) \\ \vdots \\ 0 \\ \Psi_{NP}(\mathbf{X}_J) \end{bmatrix} \quad (4.5)$$

For an easy illustration of the concept, consider a single boundary constraint $u_i(\mathbf{X}_J) = g_i(\mathbf{X}_J)$. By use of the coordinate transformation on $\delta \mathbf{d}$, the discrete equilibrium equation becomes

$$\delta \hat{\mathbf{d}}^T \hat{\mathbf{K}} \Delta \mathbf{d} = \delta \hat{\mathbf{d}}^T \Delta \hat{\mathbf{f}}; \quad \hat{\mathbf{k}} = \mathbf{\Lambda}^{-T} \mathbf{K}; \quad \Delta \hat{\mathbf{f}} = \mathbf{\Lambda}^{-T} (\mathbf{f}^{\text{ext}} - \mathbf{f}^{\text{int}}) \quad (4.6)$$

where \mathbf{K} , \mathbf{f}^{ext} , and \mathbf{f}^{int} are the stiffness matrix, external, and internal force vectors, respectively. Since the nodal value

of u_i at \mathbf{X}_J is given, $\delta \hat{d}_{ij} = 0$, and the corresponding $2(J-1) + i$ th equation of Eq. (4.6) becomes redundant and can be replaced by the constraint equation $\sum_{I=1}^{NP} \Psi_I(\mathbf{X}_J) \Delta d_{iI} = \Delta g_i(\mathbf{X}_J)$ in the following form

$$\hat{\mathcal{K}} \Delta \mathbf{d} = \Delta \hat{\mathcal{f}} \quad (4.7)$$

where

$$\hat{\mathcal{K}} = L_J^i(\hat{\mathbf{K}}) = \begin{bmatrix} \hat{\mathbf{k}}_1^T \\ \vdots \\ \hat{\mathbf{k}}_{M-1}^T \\ \boxed{\mathbf{A}_J^{iT}} \\ \hat{\mathbf{k}}_{M+1}^T \\ \vdots \\ \hat{\mathbf{k}}_{2 \times NP}^T \end{bmatrix} \leftarrow 2(J-1) + i \text{ th}; \quad (4.8)$$

$$\Delta \hat{\mathcal{f}} = \ell_J^i(\Delta \hat{\mathbf{f}}) = \begin{bmatrix} \Delta \hat{f}_1 \\ \vdots \\ \Delta \hat{f}_{M-1} \\ \boxed{\Delta g_i(\mathbf{X}_J)} \\ \Delta \hat{f}_{M+1} \\ \vdots \\ \Delta \hat{f}_{2 \times NP} \end{bmatrix} \leftarrow 2(J-1) + i \text{ th} \quad (4.9)$$

Here L_J^i is a matrix operator that replaces the $2(J-1) + i$ th row of $\hat{\mathbf{K}}$ by \mathbf{A}_J^{iT} , and ℓ_J^i is a vector operator that replaces the $2(J-1) + i$ th component of $\Delta \hat{\mathbf{f}}$ by $\Delta g_i(\mathbf{X}_J)$. In the case of multiple boundary constraints, similar procedures are repeated, and the resulting stiffness matrix and force vector are

$$\hat{\mathcal{K}} = L_{J_{NC}}^{i_{NC}} \cdots L_{J_2}^{i_2} L_{J_1}^{i_1}(\hat{\mathbf{K}}) \quad \text{and} \quad \Delta \hat{\mathcal{f}} = \ell_{J_{NC}}^{i_{NC}} \cdots \ell_{J_2}^{i_2} \ell_{J_1}^{i_1}(\Delta \hat{\mathbf{f}}) \quad (4.10)$$

where Nc is the number of constraint equations.

4.2 Mixed transformation method

The transformation method introduced in Sect. 4.1 requires the inversion of the transformation matrix. Although the inversion can be done only once at the initial stage of the incremental computation in nonlinear problems, the multiplication of matrices needs to be performed at every iteration of each load step. In this section, we introduce a mixed coordinate such that the coordinate transformation is only needed for the degrees of freedom associated with the essential and contact boundaries.

The nodes are partitioned into two groups: a boundary group G^B contains all the nodes subjected to kinematic constraints, and an interior group G^I which contains the rest of the nodes. Node numbers are re-arranged in the following way:

$$\hat{\mathbf{d}} = \begin{bmatrix} \hat{\mathbf{d}}^B \\ \hat{\mathbf{d}}^I \end{bmatrix} = \begin{bmatrix} \Lambda^{BB} & \Lambda^{BI} \\ \Lambda^{IB} & \Lambda^{II} \end{bmatrix} \begin{bmatrix} \mathbf{d}^B \\ \mathbf{d}^I \end{bmatrix} \equiv \hat{\Lambda} \mathbf{d} \quad (4.11)$$

where \mathbf{d}^B and \mathbf{d}^I are the generalized displacement vectors associated with groups G^B and G^I , respectively, and $\hat{\mathbf{d}}^B$ and $\hat{\mathbf{d}}^I$ are their nodal displacement counterparts.

Here, we introduce a mixed displacement vector \mathbf{d}^* by

$$\mathbf{d}^* = \begin{bmatrix} \hat{\mathbf{d}}^B \\ \mathbf{d}^I \end{bmatrix} = \begin{bmatrix} \Lambda^{BB} & \Lambda^{BI} \\ \mathbf{0} & \mathbf{I} \end{bmatrix} \begin{bmatrix} \mathbf{d}^B \\ \mathbf{d}^I \end{bmatrix} = \Lambda^* \mathbf{d} \quad (4.12)$$

and Λ^* and its inverse are:

$$\Lambda^* = \begin{bmatrix} \Lambda^{BB} & \Lambda^{BI} \\ \mathbf{0} & \mathbf{I} \end{bmatrix}$$

and

$$\Lambda^{*-1} = \begin{bmatrix} \Lambda^{BB^{-1}} & -\Lambda^{BB^{-1}} \Lambda^{BI} \\ \mathbf{0} & \mathbf{I} \end{bmatrix} \quad (4.13)$$

Only the inversion of Λ^{BB} is required in Eq. (4.13). The relationship between the generalized displacement, the nodal displacement, and the mixed displacement is

$$\hat{\mathbf{d}} = \hat{\Lambda} \mathbf{d} = \hat{\Lambda} \Lambda^{*-1} \mathbf{d}^* \equiv \hat{\Lambda}^* \mathbf{d}^* \quad (4.14)$$

where

$$\hat{\Lambda}^* = \hat{\Lambda} \Lambda^{*-1} = \begin{bmatrix} \mathbf{0} & \mathbf{I} \\ \Lambda^{BI} \Lambda^{BB^{-1}} & \Lambda^{II} - \Lambda^{BI} \Lambda^{BB^{-1}} \Lambda^{IB} \end{bmatrix} \quad (4.15)$$

The equilibrium equation can be transformed using a mixed coordinate for $\delta \mathbf{d}$ to yield

$$\delta \mathbf{d}^{*T} \mathbf{K}^* \Delta \mathbf{d} = \delta \mathbf{d}^{*T} \Delta \mathbf{f}^*; \quad \mathbf{K}^* = \Lambda^{*-T} \mathbf{K}; \quad \Delta \mathbf{f}^* = \Lambda^{*-T} (\mathbf{f}^{\text{ext}} - \mathbf{f}^{\text{int}}) \quad (4.16)$$

Since the constrained nodes belong to the boundary group in which the nodal values are prescribed in the mixed displacement vector, the boundary condition $u_i(\mathbf{X}_J) = g_i(\mathbf{X}_J)$ leads to $\delta d_{ij}^* = 0$, and the $2(J-1) + i$ th equation of Eq. (4.16) again becomes redundant and can be replaced by the constraint equation $\sum_{I=1}^{NP} \Psi_I(\mathbf{X}_J) \Delta d_{II} = \Delta g_i(\mathbf{X}_J)$. Following similar procedures in Eqs. (4.7)–(4.10), the incremental equilibrium equation is obtained by

$$\mathcal{H}^* \Delta \mathbf{d} = \Delta \mathbf{f}^* \quad (4.17)$$

$$\mathcal{H}^* = L_{J_{Nc}}^{i_{Nc}} \cdots L_{J_2}^{i_2} L_{J_1}^{i_1} (\mathbf{K}^*) \quad (4.18)$$

$$\delta \mathbf{f}^* = \ell_{J_{Nc}}^{i_{Nc}} \cdots \ell_{J_2}^{i_2} \ell_{J_1}^{i_1} (\delta \mathbf{f}^*) \quad (4.19)$$

where L_j^i and ℓ_j^i are the matrix and vector operators defined in Eqs. (4.8) and (4.9), respectively, following the new node numbering in the mixed coordinate system. According to Eq. (4.13), the computation in Eq. (4.16) is much less intensive than that in the full transformation method, especially when the number of boundary nodes is much smaller than the number of interior nodes.

4.3

Boundary singular kernel method

The original paper of Moving Least Squares (MLS) method by Lancaster and Salkauskas (1981) has

suggested that by introducing a singularity into the weight function, the approximation leads to interpolation. This concept was first introduced by Kaljevic and Saigal (1997) to the element free Galerkin formulation. In their approach, singular weight functions are employed at all discrete nodes, and Kronecker delta properties are recovered in the MLS shape functions. In the approach discussed herein (Chen and Wang 1999b), the reproducing kernel shape functions constructed with singularities are introduced only to the essential boundary nodes. As such, this method does not generate interpolation functions at the interior nodes or at the boundary restrained nodes, but is sufficient to obtain nodal values at the boundary restrained nodes for direct imposition of boundary conditions.

The reproducing kernel shape functions $\{\Psi_J(\mathbf{X})\}_{J=1}^{NP}$ are constructed by imposing the discrete reproducing conditions on a set of kernel functions $\{\Phi_a(\mathbf{X} - \mathbf{X}_J)\}_{J=1}^{NP}$. A singularity is introduced to the kernel function associated with a designated node I located at $\tilde{\mathbf{X}}_I$ on the essential boundary by

$$\tilde{\Phi}_a(\mathbf{X} - \tilde{\mathbf{X}}_I) = \frac{\Phi_a(\mathbf{X} - \tilde{\mathbf{X}}_I)}{f(\mathbf{X} - \tilde{\mathbf{X}}_I)} \quad (4.20)$$

where $f(\mathbf{0}) = 0$, and the superposed “ \sim ” on the nodal coordinate denoting the node with singularity imposed in the associated kernel function. The function f is chosen to have the form

$$f(\mathbf{X} - \tilde{\mathbf{X}}_I) = \left[\left(\frac{X - \tilde{X}_I}{a_x} \right)^2 + \left(\frac{Y - \tilde{Y}_I}{a_y} \right)^2 + \left(\frac{Z - \tilde{Z}_I}{a_z} \right)^2 \right]^p, \quad p > 0 \quad (4.21)$$

where $2p$ reflects the order of singularity. Following the imposition of discrete reproducing conditions discussed in Sect. 2, the reproducing kernel shape function associated with this singular kernel is

$$\tilde{\Psi}_I(\mathbf{X}) = \mathbf{H}^{[n]T}(\mathbf{0}) \tilde{\mathbf{M}}^{[n-1]}(\mathbf{X}) \mathbf{H}^{[n]}(\mathbf{X} - \tilde{\mathbf{X}}_I) \tilde{\Phi}_a(\mathbf{X} - \tilde{\mathbf{X}}_I) \quad (4.22)$$

$$\begin{aligned} \tilde{\mathbf{M}}^{[n]}(\mathbf{X}) &= \left[\sum_{J=I, J \neq I}^{NP} \mathbf{H}^{[n]}(\mathbf{X} - \mathbf{X}_J) \mathbf{H}^{[n]T}(\mathbf{X} - \mathbf{X}_J) \Phi_a(\mathbf{X} - \mathbf{X}_J) \right] \\ &\quad + \mathbf{H}^{[n]}(\mathbf{X} - \tilde{\mathbf{X}}_I) \mathbf{H}^{[n]T}(\mathbf{X} - \tilde{\mathbf{X}}_I) \Phi_a(\mathbf{X} - \tilde{\mathbf{X}}_I) \end{aligned} \quad (4.23)$$

This resulting singular kernel shape function $\tilde{\Psi}_I(\mathbf{X})$ has the property (Chen and Wang 1999b)

$$\tilde{\Psi}_I(\mathbf{X} \rightarrow \tilde{\mathbf{X}}_I) = 1 \quad (4.24)$$

Other non-singular kernel shape functions $\Psi_J(\mathbf{X})$, $J \neq I$ have the following property:

$$\Psi_J(\mathbf{X} \rightarrow \tilde{\mathbf{X}}_I) = 0 \quad (4.25)$$

The singular kernel shape function and non-singular kernel shape functions near the singular point $\tilde{\mathbf{X}}_I$ are plotted in Fig. 3. Note that $\tilde{\Psi}_I(\mathbf{X} \rightarrow \mathbf{X}_J) \neq 0$, and therefore

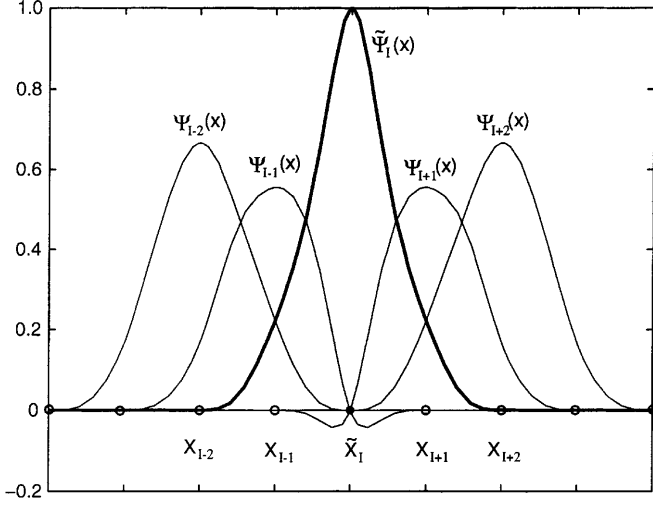


Fig. 3. Reproducing kernel shape functions associated with one singular point $\tilde{\mathbf{X}}_I$

$\tilde{\Psi}_I(\mathbf{X})$ is not an interpolation function. Recall the reproducing kernel approximation of the displacement

$$u^h(\mathbf{X}) = \left[\sum_{J=1, J \neq I}^{NP} \Psi_J(\mathbf{X}) d_J \right] + \tilde{\Psi}_I(\mathbf{X}) d_I \quad (4.26)$$

Using the properties in Eqs. (4.24) and (4.25), one can show

$$u^h(\tilde{\mathbf{X}}_I) = \left[\sum_{J=1, J \neq I}^{NP} \Psi_J(\tilde{\mathbf{X}}_I) d_J \right] + \tilde{\Psi}_I(\tilde{\mathbf{X}}_I) d_I = d_I \quad (4.27)$$

i.e., the coefficient associated with the singular kernel shape function is the nodal value of the approximated function, even though $\tilde{\Psi}_I(\mathbf{X})$ is not an interpolation function. Note that using the concept of coordinate transformation, one can show that the component of the force vector associated with the singular node is not a nodal force since Kronecker delta properties are not exactly satisfied. If singularity is introduced to all the nodes of discretization, it is clear $\tilde{\Psi}_I(\mathbf{X} \rightarrow \tilde{\mathbf{X}}_J) = \delta_{IJ} \forall I, J$.

5 Contact constraints

Contact problem is formulated by variational inequality, which is a projection of the solution onto a constraint set. Since a variational inequality problem is equivalent to a constrained minimization problem, a penalty method is often used as an approximation of a contact problem subjected to impenetration and stick constraints (Slip is treated as non-constrained condition). Consider two contacting bodies in 2-dimension, one designated as master body with domain Ω_x^M and boundary Γ_x^M , and the other designated as a slave body with domain Ω_x^S and boundary Γ_x^S as shown in Fig. 4(a). The penalized contact variational form is defined by

$$\delta \Pi + \int_{\Gamma_x^C} (\beta_n \delta \theta_n + \beta_t \delta \theta_t) d\Gamma = 0, \quad \Gamma_x^C = \Gamma_x^S \cap \Gamma_x^M \quad (5.1)$$

where $\delta \Pi$ is the virtual potential without the contribution from the contact traction, Γ_x^C is the contact surface defined as the intersection of slave surface Γ_x^S , and master surface Γ_x^M , and β_n and β_t are related to the penalty numbers:

$$\beta_n = -\omega_n \theta_n; \quad \beta_t = \begin{cases} -\omega_t \theta_t & \text{if } |\omega_t \theta_t| \leq |\mu \beta_n| \text{ (stick)} \\ -\mu \beta_n \operatorname{sgn}(\theta_t) & \text{otherwise (slip)} \end{cases} \quad (5.2)$$

where μ is the coefficient of friction, θ_n is the normal gap (negative for penetration), θ_t is the tangential relative movement, ω_n and ω_t are the penalty numbers, and Eq. (5.2) is the penalized version of the classical Coulomb law.

Figure 4b is the discretization of the potential contact surfaces with \mathbf{x}_S a designated slave node and $\mathbf{x}_{M1} - \mathbf{x}_{M2}$ a master segment closest to the slave node \mathbf{x}_S . The length ℓ , tangential unit vector \mathbf{t} , and the normal unit vector \mathbf{n} of the master segment are defined as

$$\ell = \|\mathbf{x}_{M2} - \mathbf{x}_{M1}\|, \quad \mathbf{t} = \frac{1}{\ell} (\mathbf{x}_{M2} - \mathbf{x}_{M1}), \quad \mathbf{n} = \mathbf{e}_3 \times \mathbf{t} \quad (5.3)$$

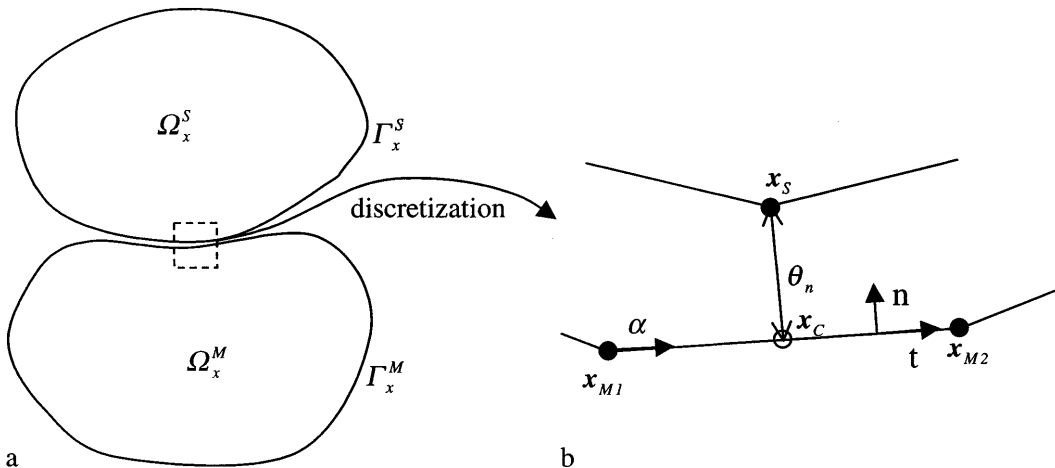


Fig. 4. Multi-body contact conditions. a Continuum contact bodies; b discrete contact surfaces

Table 1. \mathbf{K}^{tan} and $\Delta \mathbf{f}$ for different boundary condition treatments

	\mathbf{K}^{tan}	$\Delta \mathbf{f}$
Full transformation	$L_{J_1}^{i_1} \dots L_{J_n}^{i_n} (\mathbf{A}^{-\text{T}} \mathbf{K} + \hat{\mathbf{K}}^{\text{C}} \mathbf{A})$	$L_{J_1}^{i_1} \dots L_{J_n}^{i_n} [\mathbf{A}^{-\text{T}} (\mathbf{f}^{\text{ext}} - \mathbf{f}^{\text{int}}) - \hat{\mathbf{f}}^{\text{C}}]$
Mixed transformation	$L_{J_1}^{i_1} \dots L_{J_n}^{i_n} (\mathbf{A}^{*-\text{T}} \mathbf{K} + \hat{\mathbf{K}}^{\text{C}} \mathbf{A})$	$L_{J_1}^{i_1} \dots L_{J_n}^{i_n} [\mathbf{A}^{*-\text{T}} (\mathbf{f}^{\text{ext}} - \mathbf{f}^{\text{int}}) - \hat{\mathbf{f}}^{\text{C}}]$
Boundary singular kernel	$\mathbf{K} + \hat{\mathbf{K}}^{\text{C}}$	$\mathbf{f}^{\text{ext}} - \mathbf{f}^{\text{int}} - \hat{\mathbf{f}}^{\text{C}}$

where \mathbf{e}_3 is the unit vector normal pointing outward of the plane.

To introduce reproducing kernel approximation of the contact variational equation, we first consider a discretization of master surface into piecewise linear segments, and a discretization of the slave surface by a set of slave nodes. For a piecewise linear representation of the master segment, the location of the closest point projection of the slave node \mathbf{x}_S onto the master segment $\mathbf{x}_{M1} - \mathbf{x}_{M2}$, α_C , is described by the following forms:

$$\mathbf{x}_C = (1 - \alpha_C) \mathbf{x}_{M1} + \alpha_C \mathbf{x}_{M2}, \quad (5.4)$$

$$\alpha_C = (\mathbf{x}_S - \mathbf{x}_{M1}) \cdot \mathbf{t} / \ell$$

$$= [(\mathbf{X}_S - \mathbf{X}_{M1}) + (\hat{\mathbf{d}}_S - \hat{\mathbf{d}}_{M1})] \cdot \mathbf{t} / \ell \quad (5.5)$$

$$\ell = \|(\mathbf{X}_{M2} - \mathbf{X}_{M1} + (\hat{\mathbf{d}}_{M2} - \hat{\mathbf{d}}_{M1}))\| \quad (5.6)$$

where α in Fig. 4b is a natural coordinate along the master segment $\mathbf{x}_{M1} - \mathbf{x}_{M2}$, α_C is the natural coordinate of the closest point projection, and $\hat{\mathbf{d}}_S$, $\hat{\mathbf{d}}_{M1}$, and $\hat{\mathbf{d}}_{M2}$ are nodal displacement of \mathbf{x}_S , \mathbf{x}_{M1} , and \mathbf{x}_{M2} , respectively.

We also use the nodal coordinate to express normal gap θ_n and tangential relative movement θ_t

$$\theta_n = (\mathbf{x}_S - \mathbf{x}_{M1}) \cdot \mathbf{n} = (\mathbf{X}_S - \mathbf{X}_{M1}) \cdot \mathbf{n} + (\hat{\mathbf{d}}_S - \hat{\mathbf{d}}_{M1}) \cdot \mathbf{n} \quad (5.7)$$

and

$$\theta = (\alpha_C - \alpha_C^0) l^0; \quad (5.8)$$

where α_C^0 and l^0 are computed according to Eqs. (5.5) and (5.6) based on the previously converged load step.

The penalized variational equation with a collocation discretization of the contact penalty terms is

$$\delta \Pi + \sum_S (\beta_n \delta \theta_n + \beta_t \delta \theta_t)_S = 0 \quad (5.9)$$

where S is summed over the slave nodes \mathbf{x}_S when they are detected in contact with the master segments, and each term of the summation contains three unknowns $[\hat{\mathbf{d}}_S, \hat{\mathbf{d}}_{M1}, \hat{\mathbf{d}}_{M2}]$ expressed in the nodal coordinate. At each slave node \mathbf{x}_S , one can show

$$(\beta_n \delta \theta_n + \beta_t \delta \theta_t)_S = \delta \langle \hat{\mathbf{d}}_S^{\text{T}} \rangle_S (\hat{\mathbf{q}}^{\text{C}})_S \quad (5.10)$$

$$[\Delta (\beta_n \delta \theta_n + \beta_t \delta \theta_t)]_S = \delta \langle \hat{\mathbf{d}}_S^{\text{T}} \rangle_S (\hat{\mathbf{k}}^{\text{C}})_S \Delta (\hat{\mathbf{d}})_S \quad (5.11)$$

where $\langle \cdot \rangle_S$ denotes the evaluation of (\cdot) at the slave node \mathbf{x}_S , and $\langle \hat{\mathbf{d}} \rangle_S$ is a composite vector

$$\langle \hat{\mathbf{d}} \rangle_S^{\text{T}} = [\hat{\mathbf{d}}_S^{\text{T}}, \hat{\mathbf{d}}_{M1}^{\text{T}}, \hat{\mathbf{d}}_{M2}^{\text{T}}] \quad (5.12)$$

and $\hat{\mathbf{q}}^{\text{C}}$ and $\hat{\mathbf{k}}^{\text{C}}$ are the corresponding nodal contact force vector and contact stiffness matrix obtained from Eqs. (5.10) and (5.11) (Chen et al. 1998), respectively.

Using the ordering in the partitioned displacement vector $\hat{\mathbf{d}}^{\text{T}} = [\hat{\mathbf{d}}^{\text{B}^{\text{T}}}, \hat{\mathbf{d}}^{\text{T}}]$, the assembly of Eqs. (5.10) and (5.11) to the global system can be arranged as

$$\sum_S (\beta_n \delta \theta_n + \beta_t \delta \theta_t)_S = \delta \hat{\mathbf{d}}^{\text{T}} \hat{\mathbf{f}}^{\text{C}} \quad (5.13)$$

$$\sum_S [\Delta (\beta_n \delta \theta_n + \beta_t \delta \theta_t)]_S = \delta \hat{\mathbf{d}}^{\text{T}} \hat{\mathbf{K}}^{\text{C}} \Delta \hat{\mathbf{d}} \quad (5.14)$$

where

$$\hat{\mathbf{f}}^{\text{C}} = \begin{bmatrix} \mathbf{A}_S (\hat{\mathbf{q}}^{\text{C}})_S \\ \mathbf{0} \end{bmatrix} \quad (5.15)$$

$$\hat{\mathbf{K}}^{\text{C}} = \begin{bmatrix} \mathbf{A}_S (\hat{\mathbf{k}}^{\text{C}})_S & \mathbf{0} \\ \mathbf{0} & \mathbf{0} \end{bmatrix} \quad (5.16)$$

and \mathbf{A} is the assembly operator. If essential boundary conditions are imposed using the mixed transformation method, the nodes on the contact surfaces are assigned as part of the boundary group. For employment of the boundary singular kernel method, singular kernel functions are used at the potential contact nodes to construct the reproducing kernel shape functions. By following the derivation on the treatment of essential boundary conditions discussed in Sect. 4, the final incremental equation of a contact problem is generalized in the following form:

$$\mathbf{K}^{\text{tan}} \Delta \mathbf{d} = \Delta \mathbf{f} \quad (5.17)$$

where \mathbf{K}^{tan} and $\Delta \mathbf{f}$ are defined in Table 1: \mathbf{f}^{ext} , \mathbf{f}^{int} , and \mathbf{K} are associated with the discretization of external energy, internal energy, and the linearization of the potential energy, respectively, and L_j^i and ℓ_j^i are the essential boundary condition matrix and vector operators defined in Eqs. (4.8) and (4.9), respectively.

6 Numerical examples

In this section, two linear problems are first analyzed to study the convergent rates of the proposed methods, and then followed by study of nonlinear problems. The meshfree formulation for finite elasticity with pressure projection can be degenerated to a linear formulation by setting deformation gradient $\mathbf{F} = \mathbf{I}$, shear modulus $\mu = 2(A_{10} + A_{01})$, and taking k as the bulk modulus shown in Eqs. (3.25)–(3.27). The corresponding Young's modulus and Poisson's ratio can be obtained by using the relation $k = \lambda + 2\mu/3$ with λ and μ are the Lam'e constants, see Chen et al. (1999a) for details. The error norms used in the numerical study are defined as:

Displacement error norm

$$= \left[\int_{\Omega_x} (\mathbf{u}^h - \mathbf{u}^{\text{exact}}) \cdot (\mathbf{u}^h - \mathbf{u}^{\text{exact}}) d\Omega \right]^{1/2} \quad (6.1)$$

Energy error norm

$$= \left[\frac{1}{2} \int_{\Omega_x} (\boldsymbol{\varepsilon}^h - \boldsymbol{\varepsilon}^{\text{exact}}) : (\boldsymbol{\sigma}^h - \boldsymbol{\sigma}^{\text{exact}}) d\Omega \right]^{1/2} \quad (6.2)$$

We use RKPM (reproducing kernel particle method) to denote meshfree method with reproducing kernel approximation.

6.1

Inflation of a incompressible plane-strain tube

This is a standard test problem designed to identify stress oscillation and volumetric locking since the elasticity of this problem is dominated by pressure, and the constraints in axial direction further intensifies the numerical difficulty in incompressibility. An infinitely long tube, with an inner radius of 3 and an outer radius of 9, is subjected to an internal pressure as shown in Fig. 5. The material properties are $E = 100$, $\mu = 0.4999$, and pressure is $P = 1$. This problem is analyzed by an axisymmetric formulation with constraints introduced in the axial direction to impose a plane-strain condition. Several nodal refinements in the radial direction, 2×2 , 2×3 , 2×9 , 2×13 , and 2×25 , are used for convergence study. The 4-node integration zones with a 5×5 quadrature rule are used for domain integration. The analytical solution of this problem can be found in Timoshenko and Goodier (1970).

6.1.1

Treatment of incompressibility

To study the effectiveness of pressure projection (PP) method in incompressible problems, the boundary conditions are imposed by the transformation method. The displacement solutions obtained from RKPM without and with pressure projection are compared in Table 2. A severe locking is encountered without the pressure projection unless a relatively large normalized support (R) in the reproducing kernel shape function is used in the finest

Table 2. Normalized inner radial displacements predicted by RKPM without and with pressure projection

Support size R	Number of nodes				
	2×2	2×3	2×7	2×13	2×25
RKPM without pressure projection					
1.0	0.00205	0.00561	0.03890	0.13590	0.38416
2.0	0.00205	0.01182	0.16427	0.59789	0.92239
3.0	0.00205	0.01380	0.62379	0.96917	0.99683
RKPM with pressure projection					
1.0	0.88379	0.95463	0.99347	0.99831	0.99957
2.0	0.88379	0.97816	0.99860	0.99981	0.99999
3.0	0.88379	0.98098	0.99981	0.99999	1.00000

model. On the other hand, RKPM with pressure projection produces a very accurate solution even with a small support size in relatively coarse models. Radial stress solutions of a 2×25 -node model are compared in Fig. 6, and the case without pressure projection produces severe stress oscillation. It is also important to observe that, unlike the locking phenomenon, stress oscillation cannot be eliminated simply by increasing the support size of shape functions. Figure 7 compares the displacement and energy norms using the two approaches. The numbers in the figures are slopes of the lines. The locking and stress oscillation encountered in RKPM without pressure projection (PP) leads to a slower convergent rate and larger errors when compared to the case with pressure projection, especially when the normalized support size R of the shape function is small.

6.1.2

Imposition of boundary conditions

Since boundary singular kernel (BSK) method employs different shape functions on the essential boundaries, the approximation space of this approach is different from that of the full transformation method (FTM) and mixed transformation method (MTM). Note that FTM and MTM are expected to produce identical solutions, only MTM and BSK are compared in the convergence analysis. The displacement and energy norms of MTM and BSK are compared in Fig. 8. In this particular problem all the nodes are located on the boundary, therefore "boundary" singular

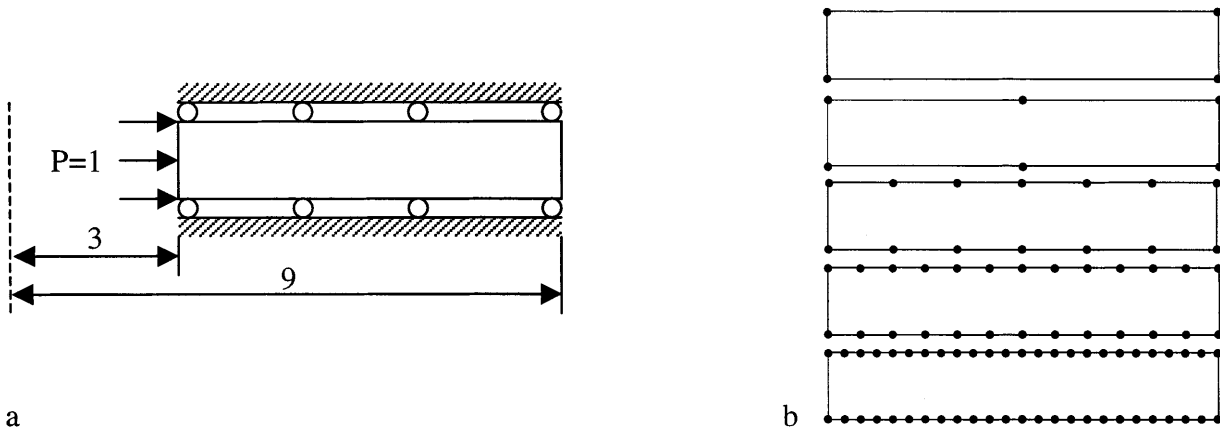


Fig. 5. Incompressible plane-strain tube subjected to internal pressure. **a** Axisymmetric plane-strain model; **b** meshfree models

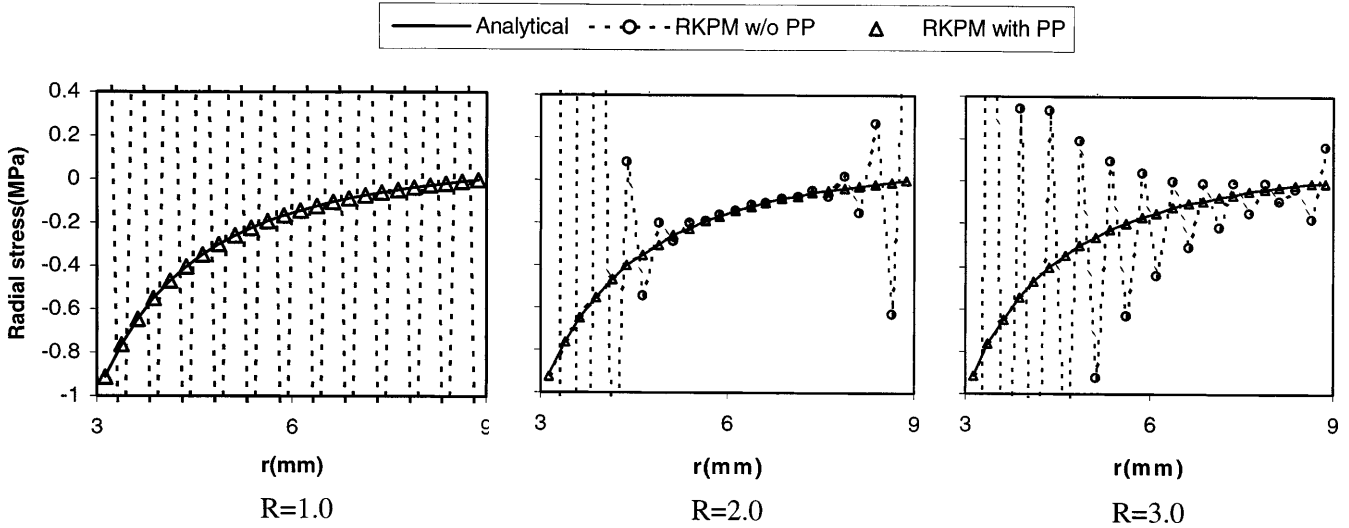


Fig. 6. Radial stress distribution predicted by RKPM without and with pressure projection

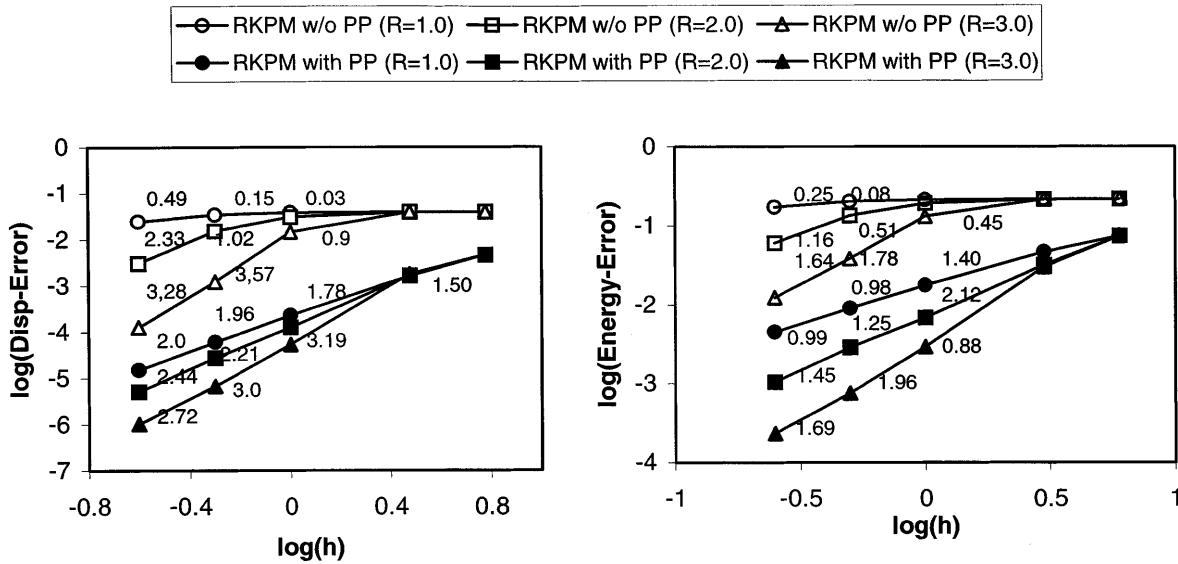


Fig. 7. Displacement and energy error norms of RKPM without and with pressure projection

kernel actually applies to all the nodes; leading to a worse rate of convergence in BSK compared to that of the MTM. Figure 9 compares the radial stresses of a 2×25 -node model MTM and BSK, and the results of the two methods are almost indistinguishable for normalized support sizes of $R = 1.0, 2.0, 3.0$. The CPU comparison is given in Table 3. Due to the fact that all the nodes are on the boundary in this problem, there is virtually no difference in computation time between FTM and MTM since the sizes of the transformation matrices for the two methods are identical. The reduction of CPU in BSK is also marginal in this case.

6.2 Pressure-loaded half plane

The convergence properties of the pressure projection method and boundary singular kernel method are further studied in this problem. The problem statement and

Table 3. Normalized CPU time comparison in tube inflation problem

R	Full transformation	Mixed transformation	Boundary singular kernel
1.0	1.00	1.00	0.71
2.0	2.14	2.14	1.86
3.0	3.86	3.86	3.57

numerical model of 3×3 region which takes into account symmetry and boundary traction (h_x, h_y) from analytical solution are shown in Fig. 10 (following Beissel et al., 1996). The material properties are $E = 100$ and $\mu = 0.4999$, and the pressure load is $P = 1$. The nodes are completely fixed along $x = 3$, and the surface traction is prescribed along $y = -3$ according to the analytical solution. Several levels of nodal refinements for convergence study are shown in Fig. 11.

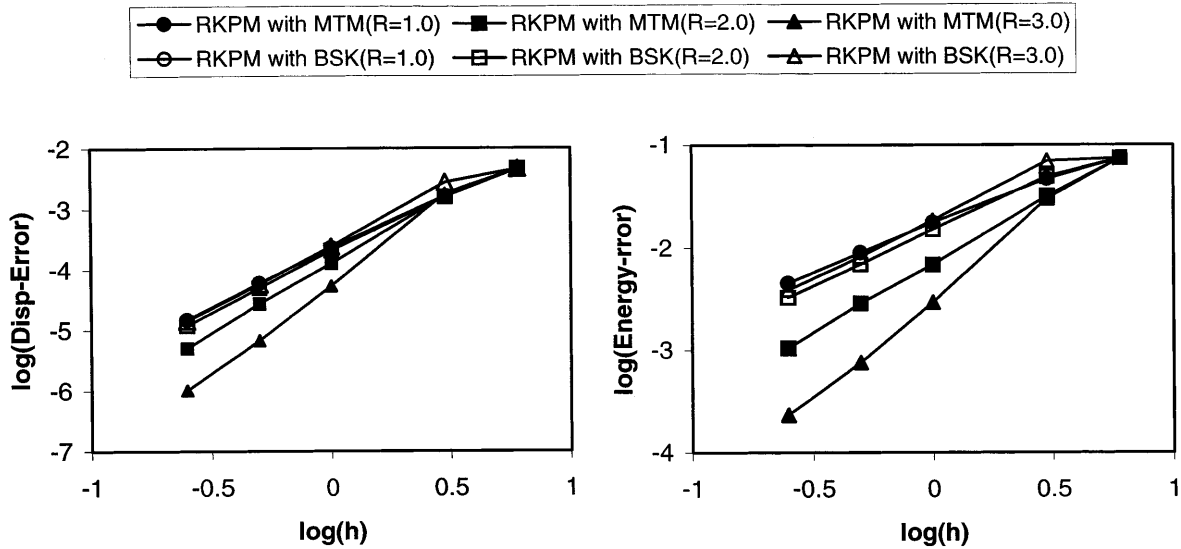


Fig. 8. RKPM displacement and energy error norms using a mixed transformation method (MTM) and a boundary singular kernel (BSK) method

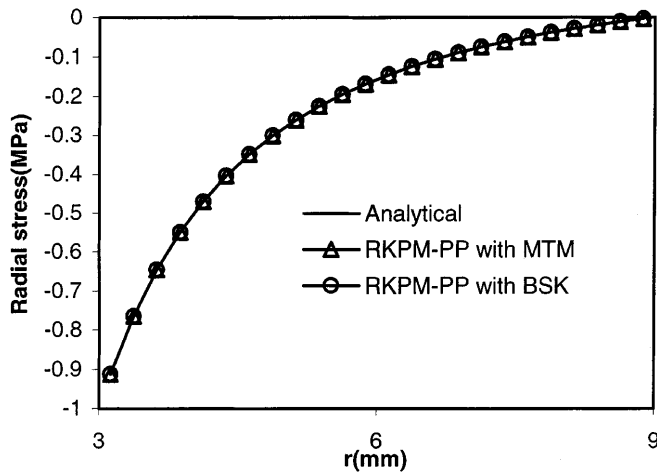


Fig. 9. Radial stress distribution predicted by RKPM using a mixed transformation method (MTM) and a boundary singular kernel (BSK) method

6.2.1

Treatment of incompressibility

To identify the numerical difficulties associated with incompressibility in RKPM, the boundary conditions are imposed using the transformation method in this study. Figure 12 compares the displacement and energy error norms of RKPM without and with pressure projection (PP) using nodal refinements displayed in Fig. 11. The convergent rate of displacement and energy norms of the case without pressure projection is particularly low when the normalized support size R is small. Using the pressure projection method, the displacement and energy errors are significantly reduced, and the rates of convergence are increased. The y -normal stress results of the 16×16 -node model compared in Fig. 13 show that the stress oscillation is severe without the pressure projection, and the increase of support size R actually results in a more severe stress oscillation. The stress oscillation is effectively eliminated with the pressure

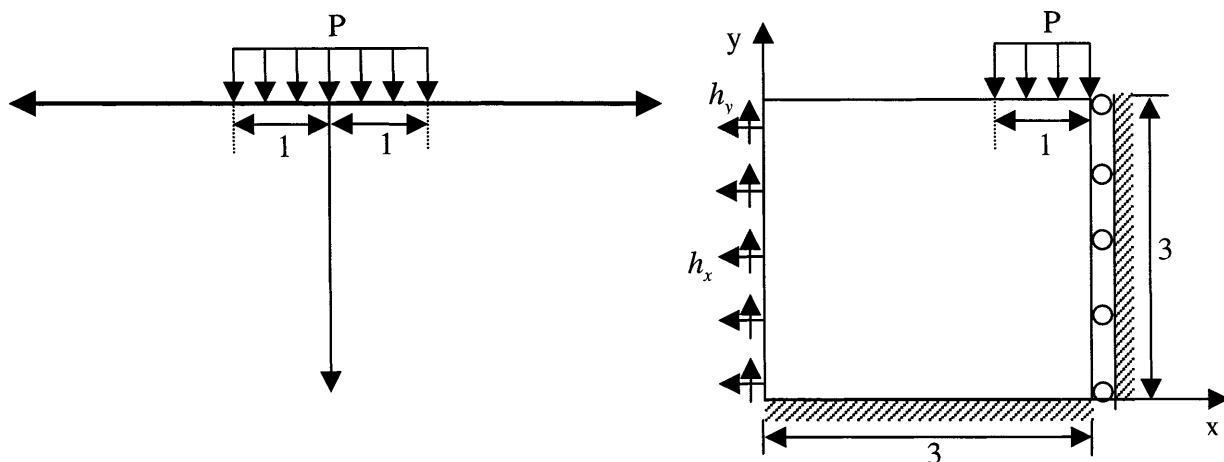


Fig. 10. Problem statement of a pressure-loaded half plane

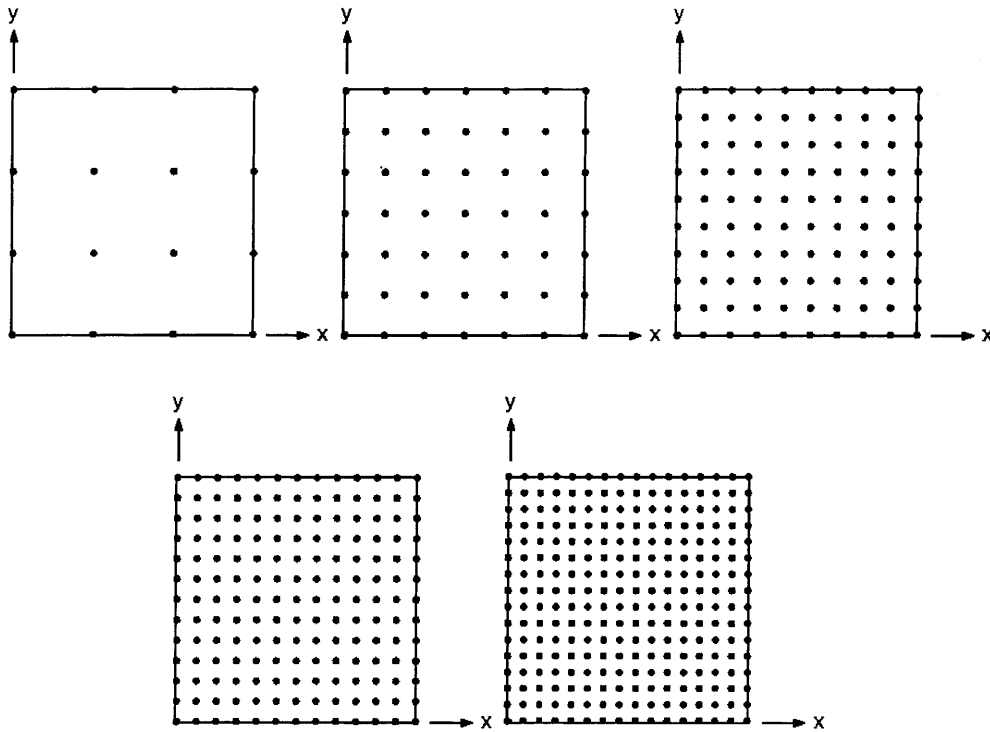


Fig. 11. Meshfree models for the pressure-loaded half plane problem

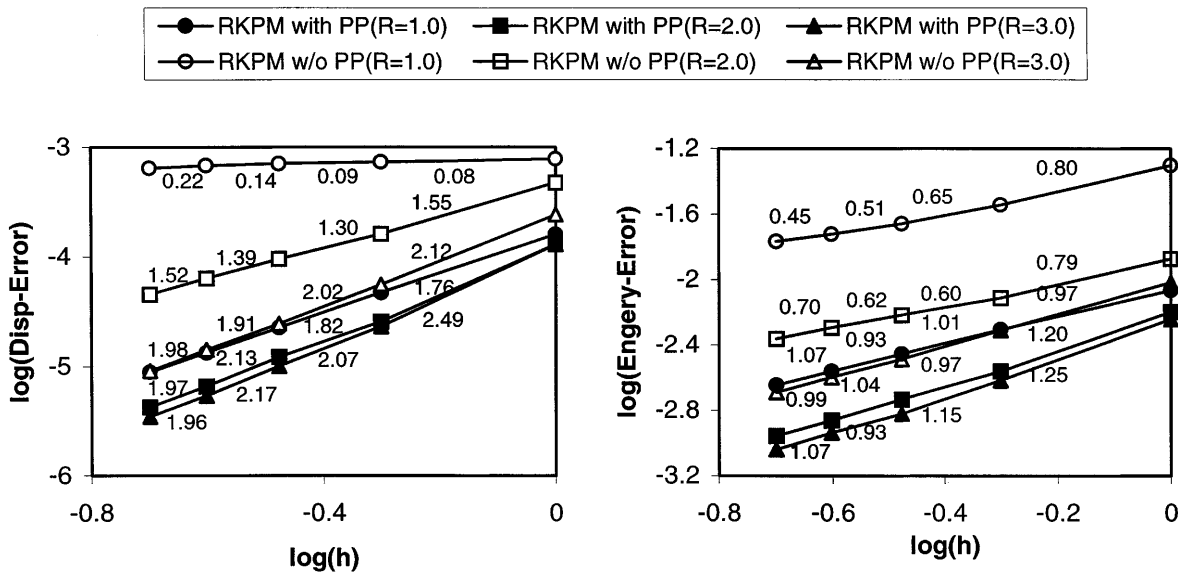


Fig. 12. Displacement and energy error norms of RKPM without and with pressure projection

projection method and it performs well regardless of the support size.

6.2.2

Imposition of essential boundary conditions

For a clear examination of the effectiveness and convergence properties of different boundary condition treatments, the pressure projection method is employed to avoid locking and pressure oscillation in the following analysis. Note that the full transformation method (FTM) and mixed transformation method (MTM) are expected to

generate identical numerical solutions, and therefore only MTM and boundary singular kernel (BSK) method are compared in the convergence analysis. The error norms of the RKPM using BSK are compared with those obtained from the MTM in Fig. 14. The results show that when the normalized support size R is smaller than 3.0, the two approaches perform equally well. Accuracy and convergent rate in the BSK approach start to deteriorate when the normalized support size is larger than 3.0. The y -normal stress solutions of the 16×16 -node model shown in Fig. 15 indicates a small stress oscillation near the

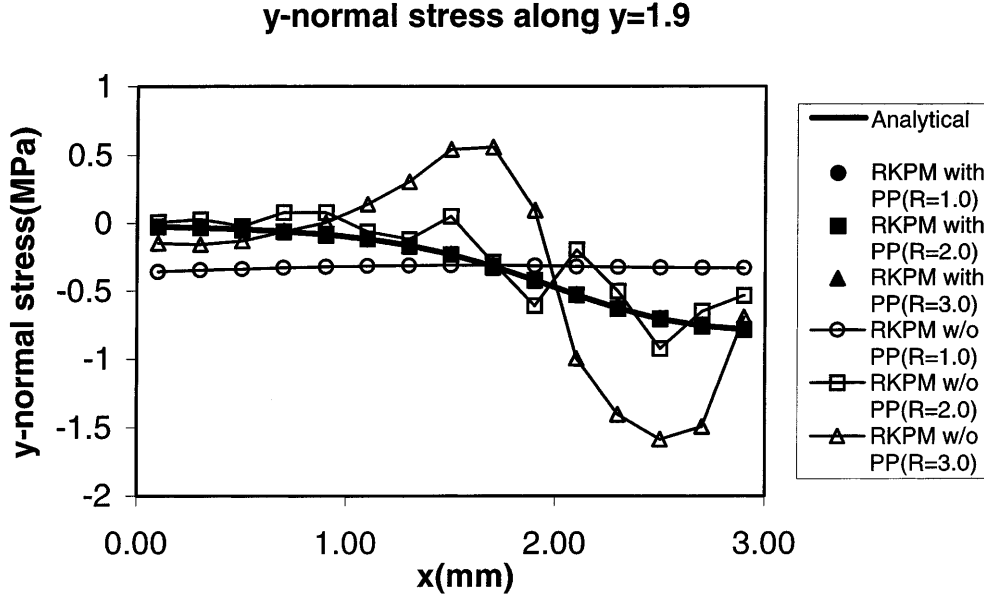


Fig. 13. Y-normal stress distribution by RKPM without and with pressure projection

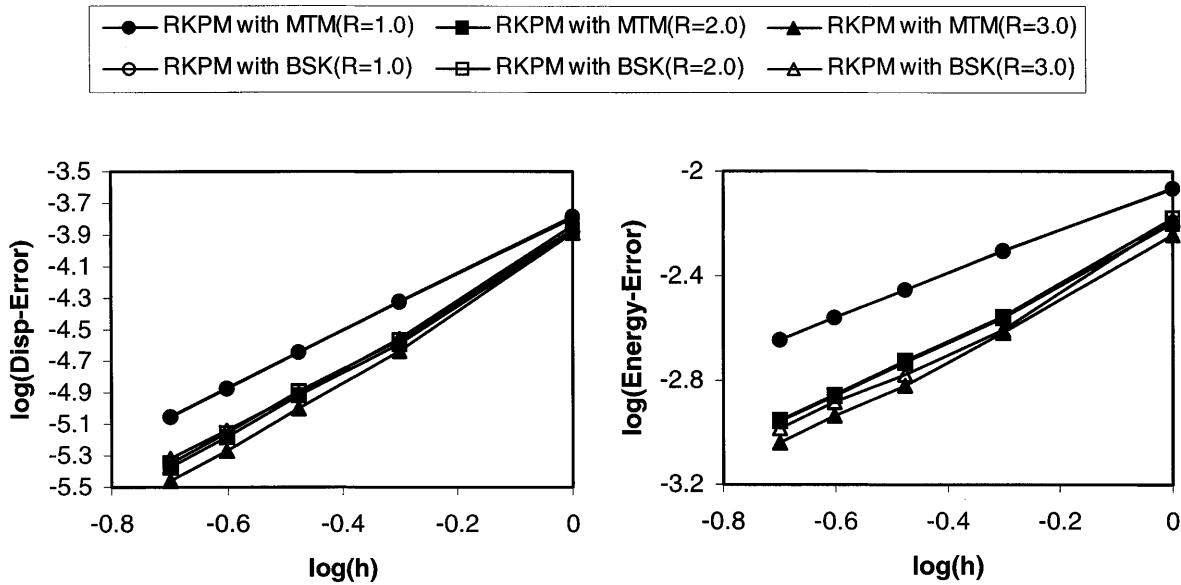


Fig. 14. RKPM displacement and energy error norms using a mixed transformation method (MTM) and a boundary singular kernel (BSK) method

boundary when the normalized support size $R = 3.0$ is employed using the BSK method. While the accuracy of BSK is comparable to the transformation methods, a substantial time saving is achieved in MTM and BSK as shown in Table 4.

6.3 Rubber ring compression

6.3.1 Plane-strain Mooney-Rivlin rubber ring

A plane-strain rubber ring, with inner radius 4.14 cm and outer radius 6.35 cm is compressed between two rigid plates as shown in Fig. 16. The following strain energy density function is used to describe the nearly incompressible hyperelastic behavior of rubber:

$$W = \sum_{i+j=1}^{\infty} A_{ij}(\bar{I}_1 - 3)(\bar{I}_3 - 3) + \frac{k}{2}(J - 1)^2 \quad (6.3)$$

where \bar{I}_1 and \bar{I}_2 are defined in Eq. (3.5), and the materials properties are $A_{10} = 40.68 \text{ N/cm}^2$, $A_{01} = 10.17 \text{ N/cm}^2$ and $k = 10^5 \text{ N/cm}^2$. The large value of $k/(A_{10} + A_{01})$ imposes incompressibility to the problem. Up to 5.08 cm of the relative vertical displacements between the plates are prescribed. Frictional contact between the rubber ring and the rigid plates is considered with coefficient of friction $\mu = 0.4$, and contact penalty numbers are set to be $\omega_n = \omega_t = 10^7$.

Three model refinements as shown in Fig. 16 are used in the numerical study. Figure 17 shows that the use of a coarse model (model 1) leads to a locking situation when the pressure projection method is not employed in

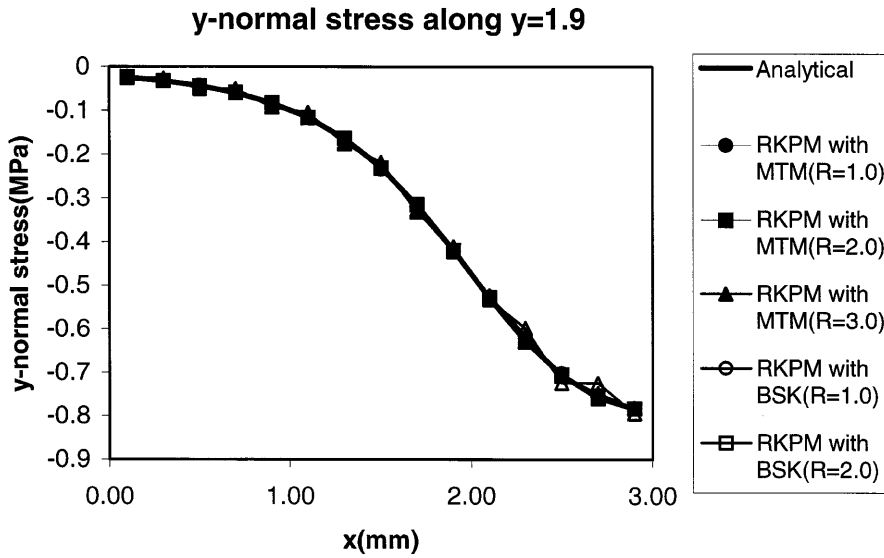


Fig. 15. Y-normal stress distribution predicted by RKPM using a mixed transformation method (MTM) and a boundary singular kernel (BSK) method

Table 4. Normalized CPU time comparison in a pressure loaded half-plane problem

R	Full transformation	Mixed transformation	Boundary singular kernel
1.0	1.00	0.53	0.45
2.0	1.10	0.65	0.54
3.0	1.44	0.97	0.86

RKPM. Locking can be resolved either by increasing the shape function support size (Fig. 17) or by refining the model (Fig. 18), but both are costly. With the employment of pressure projection, locking is removed, and accurate solution can be obtained with coarse model and with small supports, and this significantly increases efficiency.

6.3.2 Plane-stress polyurethane rubber ring

The experimentally measured load-displacement response of a polyurethane rubber ring under compression (Dureli and Parks 1970) is compared to examine the effectiveness of the proposed boundary condition treatments. Because the thickness (1.27 cm) of the ring specimen is smaller than the planner dimensions, a two-dimensional, plane-stress condition is assumed. The Saint Venant-Kirchhoff strain energy density function is used to describe the nonlinear behavior of the polyurethane rubber:

$$W = \frac{1}{2} C_{ijkl} E_{ij} E_{kl}; \quad C_{ijkl} = \lambda \delta_{ij} \delta_{kl} + \mu (\delta_{ik} \delta_{jl} + \delta_{il} \delta_{jk}) \quad (6.4)$$

where E is the Green Lagrangian strain, and λ and μ are Lam'e constants. The material properties of the test

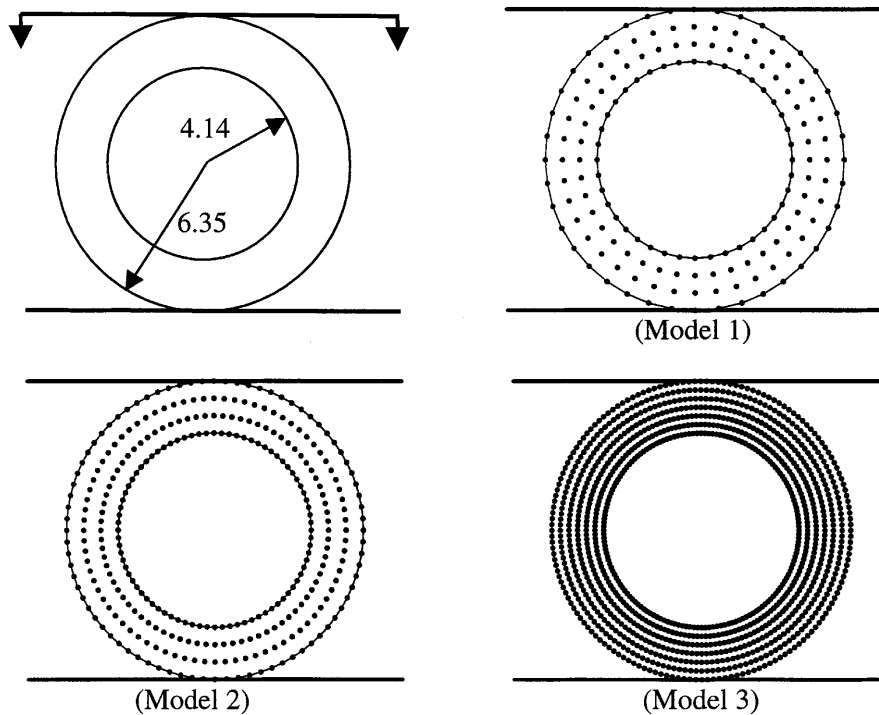


Fig. 16. Undeformed configuration and meshfree model of the ring compression problem

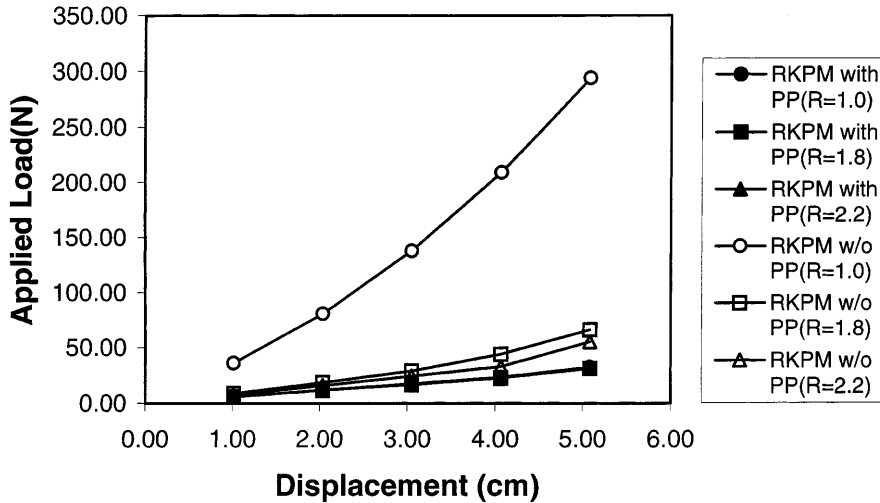


Fig. 17. RKPM analysis of tube compression without and with pressure projection: effect of shape function support size (using model 1)

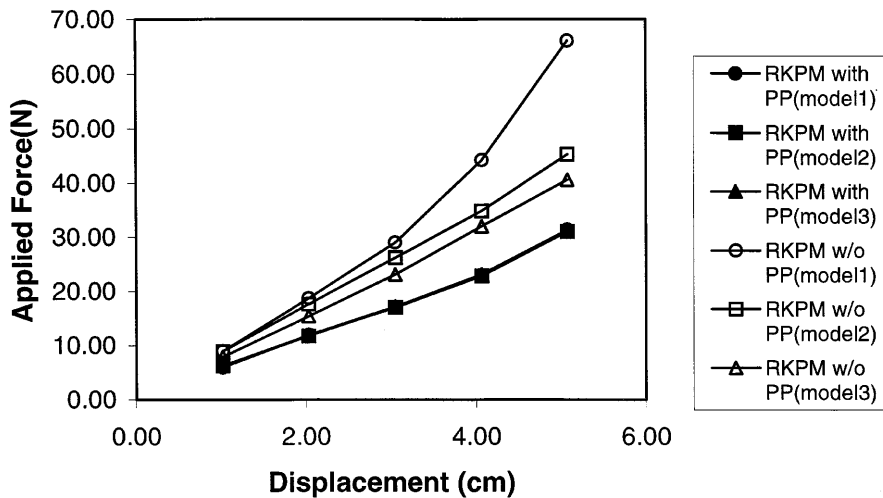


Fig. 18. RKPM analysis of tube compression without and with pressure projection: effect of model refinement (using $R = 1.8$)

specimen (Dureli and Parks 1970) are $E = 406.79 \text{ N/cm}^2$, $\nu = 0.48$. Frictional contact between the rubber ring and the rigid plates is considered with the coefficient of friction $\mu = 0.4$, and contact penalty numbers are set to be $\omega_n = \omega_t = 10^7$.

Model 3 with 287 nodes is used to compare the RKPM solution using the transformation methods and the boundary singular kernel method, and the normalized shape function support size of $R = 2.0$ is employed. Up to 5.08 cm of the relative vertical displacements between the plates are prescribed using five equal incremental steps. The computed load-deflection results obtained from different boundary condition treatments are compared favorably with experimental data in Fig. 19, and the ring deformations are plotted in Fig. 20. In this problem 78 out of 287 nodes belong to the boundary group, and the mixed transformation method and the boundary singular kernel method reduce 68% and 72% CPU time of that in the full transformation method as shown in Table 5.

6.4

Engine mount

The engine mount geometry and the associated loading conditions are described in Fig. 21. In this problem, the

outer metal casing and the inner metal piece are treated as rigid bodies, and only the rubber materials are modeled. The outer surface of the rubber model is completely fixed, and the interfaces between the rubber components and the inner metal piece are moved downward as rigid surfaces. The rubber properties of Eq. (6.3) are $A_{10} = 0.145 \text{ MPa}$, $A_{01} = 0.062 \text{ MPa}$, and $k = 6900 \text{ MPa}$. A 9-node finite element mesh is generated for comparison of finite element and meshfree solution. Two RKPM models are generated using finite element mesh as the integration zones for RKPM computation as shown in Fig. 21.

The RKPM analysis without pressure projection is first performed using a coarse model and a refined model with shape function support size $a = 0.46$. Since high material distortion near the lower corner of the lower rubber leg is expected, a larger dilation parameter $a = 0.66$ is used near this corner area. The coarse model without the employment of pressure projection (PP) leads to a locking situation as shown in Fig. 22. With the use of a refined model, locking is relieved and softer response is obtained. On the other hand, by employing pressure projection in the RKPM formulation, the use of coarse model is capable of obtaining a solution close to the much refined the RKPM solution without pressure projection. A 619-node Finite

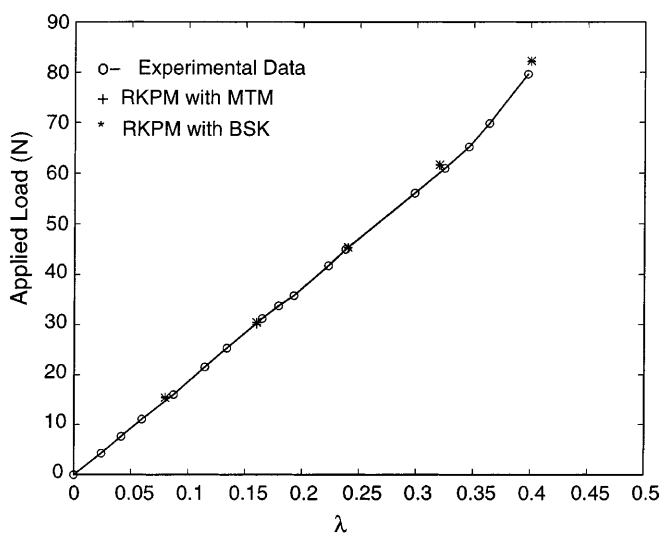


Fig. 19. Load-displacement of the polyurethane rubber ring under compression

Element model using a 9-node mixed formulation with a linear pressure field (Chen et al. 1996a) generates a very similar result as that of the RKPM solution. However, Finite Element Computation diverged at an early stage due to the mesh distortion near the corners of rubber legs. As can be seen in the deformation plots shown in Fig. 23, the localized buckling is very well captured by the RKPM with pressure projection. Severe pressure oscillation in the solution of the RKPM method is totally eliminated using pressure projection as shown in Fig. 24. In this problem the three boundary condition treatments generate almost identical results, and the CPU time comparison is given in Table 6.

Table 5. CPU comparison of the polyurethane rubber ring under compression

Full transformation	Mixed transformation	Boundary singular kernel
1.0	0.32	0.28

7 Conclusions

Several enhancements in meshfree methods for incompressible small/finite strain elasticity problems have been presented. The first improvement is to cure the deficiency in the meshfree discretization of an incompressibility constraint in a boundary value problem. Due to the employment of higher-order shape functions in the meshfree formulation, higher-order quadrature rules are required when the Gauss integration method is employed. This leads to an over-constrained discrete system in the meshfree discretization, and volumetric locking and pressure oscillation are consequences of an over-constrained discrete system. Such numerical defect can be corrected by increasing the degree of dependency in the discrete constraint equations to relax the over-constrained situation. This can be achieved by enlarging the support size of the meshfree shape functions, but the high computational costs make this simple approach unattractive. The numerical observation also shows that although locking can be effectively removed with an increase of support sizes, no improvement was found in reducing pressure oscillation.

An alternative approach is to project pressure, which is a bi-product of the incompressibility constraint, onto a lower-order space to reduce the number of independent discrete incompressibility constraints. The projection is

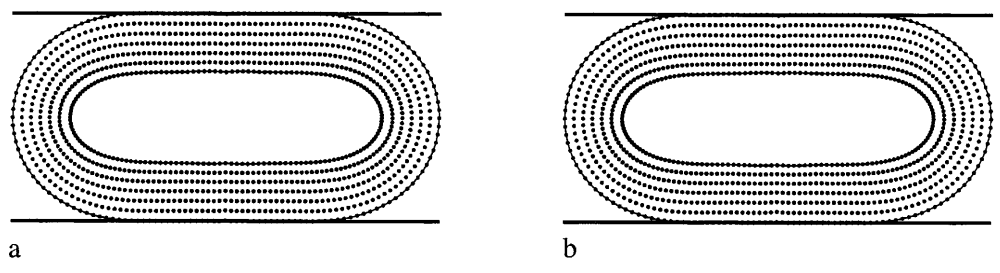


Fig. 20 a, b. Deformed geometries of the polyurethane rubber ring under compression. a mixed transformation method; b boundary singular kernel method

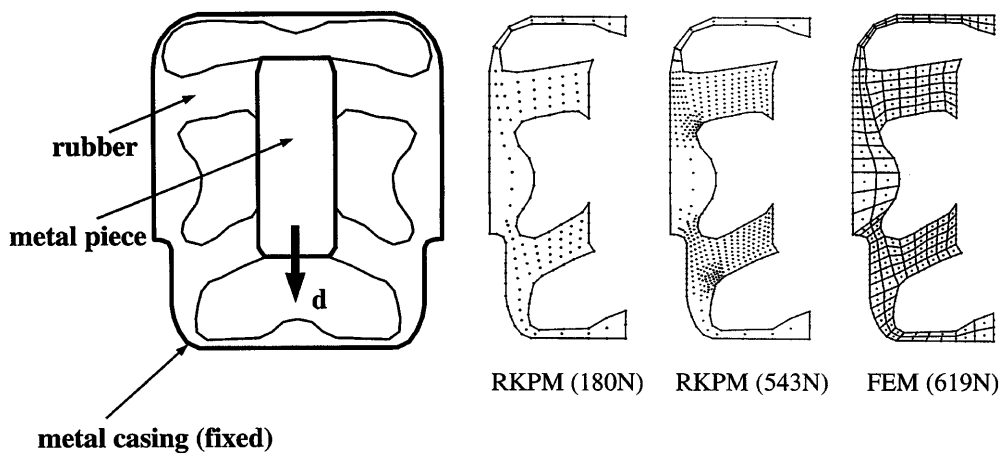


Fig. 21. Engine mount problem statement and analysis models

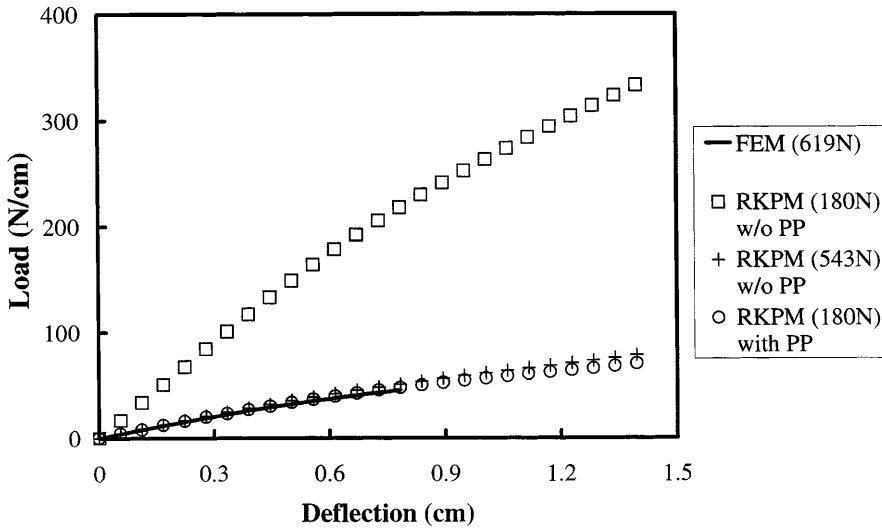


Fig. 22. Engine mount load-displacement curves by RKPM and FEM

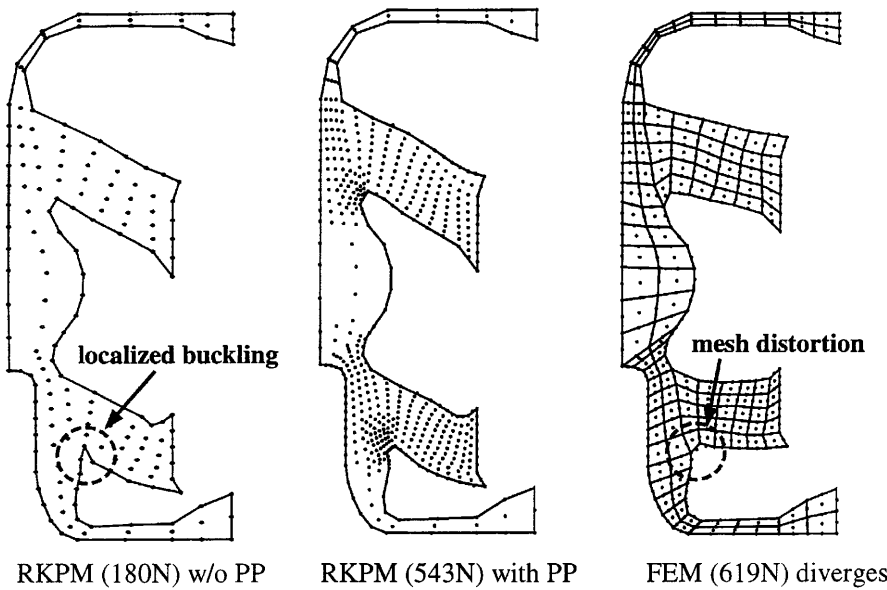


Fig. 23. Deformed geometries of engine mount predicted by RKPM and FEM

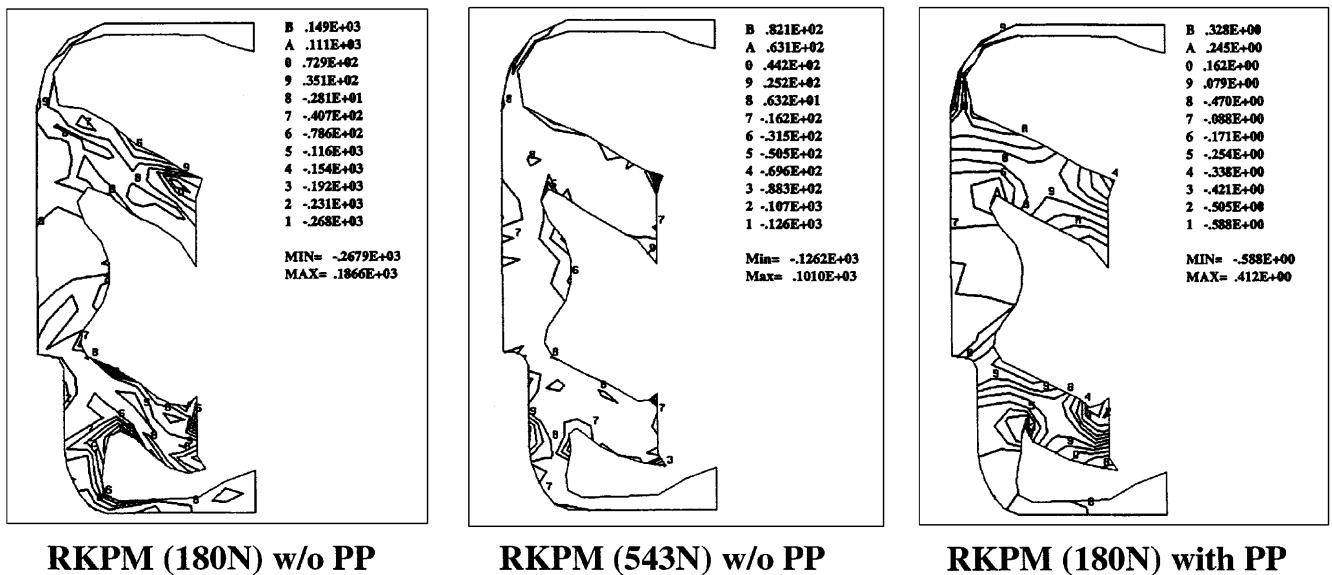


Fig. 24. Pressure distribution predicted by RKPM without and with pressure projection

Table 6. Normalized CPU time comparison in an engine mount problem

Full transformation	Mixed transformation	Boundary singular kernel
1.00	0.73	0.58

accomplished by a least-squares L_2 projection locally at each integration zone of the meshfree discretization. The numerical results show that pressure projection effectively resolves locking and pressure oscillation difficulties.

Convergent rates are increased substantially especially when small support sizes in the shape functions are used. With this approach, high accuracy can be obtained without the need of using large support size in the meshfree shape functions, and thereby significantly improves the computational efficiency.

Several methods were presented to improve the time consuming boundary condition procedures in meshfree discretization of boundary value problems. To avoid the use of a Lagrange multiplier method that involves additional unknowns, a transformation method was first introduced. The nodes in meshfree discretization are partitioned into essential boundary nodes and the interior nodes. A mixed coordinate is introduced so that only the essential boundary nodes are expressed in nodal coordinate. The size of the corresponding transformation matrix is reduced since it is only proportional to the displacement degrees of freedom on the essential boundary. Consequently, coordinate transformation can be performed effectively to provide a direct imposition of boundary conditions. Another attempt to simplify boundary condition imposition is to introduce singularity to the kernel functions associated with the boundary constrained nodes. Although Kronecker properties are not recovered with this approach, the coefficients associated with the boundary nodes become nodal values and therefore essential boundary conditions can be imposed directly. While this approach completely removes the need of coordinate transformation or the solution of Lagrange multipliers, we are concerned whether the numerical performance of meshfree approximation will be deteriorated when singular kernel functions are used to construct meshfree shape functions for the essential boundary nodes. The numerical convergence study suggests that as long as the normalized support size of the meshfree shape function stays within about 3, no deterioration in the accuracy and rate of convergence is experienced. Contact constraints can be easily implemented with the standard procedures using the proposed transformation and boundary singular kernel methods. Numerical examples of contact and small/finite strain elasticity problems demonstrate the effectiveness of the proposed boundary condition treatments.

References

Atluri SN, Reissner E (1989) On the formulation of variational theorems involving volume constraints. *Comput. Mech.* 5:337–344

Atluri SN, Zhu T (1998a) A new meshless local Petrov-Galerkin (MLPG) approach. *Comput. Mech.* 22:117–127

Atluri SN, Zhu T (1998b) A new meshless local Petrov-Galerkin (MLPG) approach to nonlinear problems. *Comp. Modeling and Simulation in Eng.* 3:187–196

Babuska I (1973) The finite element method with Lagrangian multipliers. *Num. Math.* 20:179–192

Beissel S, Belytschko T (1996) Nodal integration of the element-free Galerkin method. *Comput. Meth. Appl. Mech. Eng.* 139:49–74

Belytschko T, Ong JS-J, Liu WK, Kennedy JM (1984) Hourglass control in linear and nonlinear problems. *Comput. Meth. Appl. Mech. Eng.* 43:251–276

Belytschko T, Bachrach WE (1986) Efficient implementation of quadrilaterals with high coarse-mesh accuracy. *Comput. Meth. Appl. Mech. Eng.* 54:279–301

Belytschko T, Lu YY, Gu L (1994) Element-free Galerkin methods. *Int. J. Num. Meth. Eng.* 37:229–256

Belytschko T, Tabarra M (1996a) Dynamic fracture using element-free Galerkin methods. *Int. J. Num. Meth. Eng.* 39:923–938

Belytschko T, Kronggauz Y, Organ D, Fleming M (1996b) Meshless methods: An overview and recent developments. *Comput. Meth. Appl. Mech. Eng.* 139:3–47

Brezzi F (1974) On the existence, uniqueness and approximation of saddle-point problems arising from Lagrangian multipliers. *R.A.I.R.O. Num. Anal.* 8:129–151

Chang TYP, Saleeb AF, Li G (1991) Large strain analysis of rubber-like materials based on a perturbed Lagrangian variational principle. *Comput. Mech.* 8:221–233

Chen JS, Pan C, Wu CT (1996a) A pressure projection method for nearly incompressible rubber hyperelasticity, Part I: Theory, Part II: Applications. *J. Appl. Mech.* 63:862–876

Chen JS, Pan C, Wu CT, Liu WK (1996b) Reproducing kernel particle methods for large deformation analysis of nonlinear structures. *Comp. Meth. Appl. Mech. Eng.* 139:195–227

Chen JS, Han W, Wu CT, Duan W (1997a) On the perturbed Lagrangian formulation for nearly incompressible and incompressible hyperelasticity. *Comp. Meth. Appl. Mech. Eng.* 142:335–351

Chen JS, Pan C, Wu CT (1997b) Large deformation analysis of rubber based on a reproducing kernel particle method. *Comput. Mech.* 19:211–227

Chen JS, Pan C, Roque CMOL, Wang HP (1998) A Lagrangian reproducing kernel particle method for metal forming analysis. *Comput. Mech.* 22:289–307

Chen JS, Yoon S, Wang HP, Liu WK (1999a) An improved reproducing kernel particle method for nearly incompressible finite elasticity solids (in press). *Comp. Meth. Appl. Mech. Eng.*

Chen JS, Wang HP (1999b) New boundary condition treatments for meshless computation of contact problems (in press). *Comp. Meth. Appl. Mech. Eng.*

Dureli AJ, Parks VJ (1970) *Moire Analysis of Strains*. Prentice-Hall, Englewood Cliffs, NJ

Duarte CAM, Oden JT (1995) *HP Clouds – A Meshless Method to Solve Boundary Value Problems*, Technical Report 95-05, TICAM, The University of Texas at Austin

Duarte CAM, Oden JT (1996) A h-p adaptive method using clouds. *Comp. Meth. Appl. Mech. Eng.* 139:237–262

Flanagan DP, Belytschko T (1981) A uniform strain hexahedron and quadrilateral with orthogonal hourglass control. *Int. J. Num. Meth. Eng.* 17:679–706

Gunther F, Liu WK (1998) Implementation of boundary conditions for meshless methods. *Comp. Meth. Appl. Mech. Eng.*, submitted

Hughes TJR (1980) Generalization of selective integration procedures to anisotropic and nonlinear media. *Int. J. Num. Meth. Eng.* 15:1413–1418

Hughes TJR (1987) *The Finite Element Method*, Prentice-Hall, NJ

Kaljevic I, Saigal S (1997) An improved element free Galerkin formulation. accepted, *Int. J. Num. Meth. Eng.* 40:2953–2974

- Krongauz Y, Belytschko T** (1996) Enforcement of essential boundary conditions in meshless approximations using finite elements. *Comp. Meth. Appl. Mech. Eng.* 131:133–145
- Lancaster P, Salkauskas K** (1981) Surfaces generated by moving least squares methods. *Math. Comput.* 37:141–158
- Li S, Liu WK** (1998) Synchronized reproducing kernel interpolant via multiple wavelet expansion. *Comput. Mech.* 21:28–47
- Li S, Liu WK** (1999) Reproducing kernel hierarchical partition of unity. Part I: Formulation and theory, Part II: Applications. *Int. J. Num. Meth. Eng.* 45:251–317
- Liu WK, Ong JS-J, Uras RA** (1985) Finite element stabilization matrices – a unification approach. *Comp. Meth. Appl. Mech. Eng.* 53:13–46
- Liu WK, Belytschko T, Chen JS** (1988) Nonlinear versions of flexurally superconvergent elements. *Comp. Meth. Appl. Mech. Eng.* 71:241–258
- Liu WK, Jun S, Zhang YF** (1995) Reproducing kernel particle methods. *Int. J. Num. Meth. Fluids.* 20:1081–1106
- Liu WK, Chen Y, Chang CT, Belytschko T** (1996a) Advances in multiple scale kernel particle methods. *Comput. Mech.* 18(2):31–111
- Liu WK, Chen Y, Uras RA, Chang CT** (1996b) Generalized multiple scale reproducing kernel particle methods. *Comp. Meth. Appl. Mech. Eng.* 139:91–158
- Liszka TJ, Duarte CAM, Tworzydło WW** (1996) hp-meshless cloud method. *Comput. Meth. Appl. Mech. Eng.* 139:263–288
- Lu YY, Belytschko T, Gu L** (1994) A new implementation of the element free Galerkin method. *Comp. Meth. Appl. Mech. Eng.* 113:397–414
- Malkas DS, Hughes TJR** (1978) Mixed finite element methods-reduced and selective integration techniques: A unification of concepts. *Comp. Meth. Appl. Mech. Eng.* 15:63–81
- Melenk JM, Babuska I** (1996) The partition of unity finite element method: Basic theory and applications. *Comp. Meth. Appl. Mech. Eng.* 139:289–314
- Herrmann LR** (1965) Elasticity equations for incompressible and nearly incompressible materials by a variational theorem. *AIAA J.* 3:1896–1900
- Simo JC, Taylor RL, Pister KS** (1985) Variational and projection methods for volume constraint in finite deformation elastoplasticity. *Comp. Meth. Appl. Mech. Eng.* 51:177–208
- Scharnhorst T, Pian THH** (1978) Finite element analysis of rubber-like materials by a mixed model. *Int. J. Num. Meth. Eng.* 12:665–676
- Sussman TS, Bathe KJ** (1987) A finite element formulation for incompressible elastic and inelastic analysis. *Comput. Struct.* 26:357–409
- Timoshenko SP, Goodier JN** (1970) *Theory of Elasticity*, 3rd Edition, McGraw-Hill, NY
- Zhu T, Atluri SN** (1998) A modified collocation method and a penalty formulation for enforcing the essential boundary conditions in the element free Galerkin method. *Comput. Mech.* 21:211–222